

On the Sensing Performance of OFDM-based ISAC under the Influence of Oscillator Phase Noise

Lucas Giroto de Oliveira, *Graduate Student Member, IEEE*, Yueheng Li, Benedikt Geiger, *Graduate Student Member, IEEE*, Laurent Schmalen, *Fellow, IEEE*, Thomas Zwick, *Fellow, IEEE*, and Benjamin Nuss, *Senior Member, IEEE*

Abstract—Integrated sensing and communication (ISAC) is a novel capability expected for sixth generation (6G) cellular networks. To that end, several challenges must be addressed to enable both mono- and bistatic sensing in existing deployments. A common impairment in both architectures is oscillator phase noise (PN), which not only degrades communication performance, but also severely impairs radar sensing. To enable a broader understanding of orthogonal-frequency division multiplexing (OFDM)-based sensing impaired by PN, this article presents an analysis of sensing performance in OFDM-based ISAC for different waveform parameter choices and settings in both mono- and bistatic architectures. In this context, the distortion of the adopted digital constellation modulation is analyzed and the resulting PN-induced effects in range-Doppler radar images are investigated both without and with PN compensation. These effects include peak power loss of target reflections and higher sidelobe levels, especially in the Doppler shift direction. In the conducted analysis, these effects are measured by the peak power loss ratio, peak-to-sidelobe level ratio, and integrated sidelobe level ratio parameters, the two latter being evaluated in both range and Doppler shift directions. In addition, the signal-to-interference ratio is analyzed to allow not only quantifying the distortion of a target reflection, but also measuring the interference floor level in a radar image. The achieved results allow to quantify not only the PN-induced impairments to a single target, but also how the induced degradation may impair the sensing performance of OFDM-based ISAC systems in multi-target scenarios.

Index Terms—6G, bistatic sensing, integrated sensing and communication (ISAC), millimeter wave (mmWave), monostatic sensing, orthogonal frequency-division multiplexing (OFDM), oscillator phase noise (PN).

I. INTRODUCTION

ONE of the most anticipated features of future sixth generation (6G) cellular networks is integrated sensing and communication (ISAC) [1], [2], which is expected to be addressed already in the early releases of 3rd Generation Partnership Project (3GPP) specifications for 6G. Supported by robust connectivity at high data rates [3], [4], ISAC is

expected to enable a wide range of environment sensing use cases [5], [6]. An example is performing radar measurements with existing cellular network deployments to contribute to the maintenance of real-time digital twins of the physical wireless environment. These can, in turn, be used to coordinate and optimize the performance of both communication and sensing subsystems [7], [8].

Enabling radar sensing as an additional functionality in cellular networks comes with a series of challenges and requirements [9], [10]. In quasi-monostatic sensing architectures, henceforth referred to as monostatic for conciseness, in-band full duplex (IBFD) operation [11] is required. This results in the need of high isolation between the closely located transmitter and receiver antenna arrays, besides self-interference cancellation (SIC) at both radio-frequency (RF) and baseband (BB) stages to avoid degrading the communication performance and reducing the sensing dynamic range of the ISAC system [12], [13]. In bi- and multistatic architectures [14]–[18], inherent challenges from radar networks [19] such as time, frequency, and sampling frequency offsets are observed [20]–[22]. Although synchronization is possible with already existing fifth generation (5G) cellular resources [23], much finer accuracy is demanded for radar sensing than for communication [24].

Although the three aforementioned synchronization mismatches are only relevant when performing sensing between two distinct nodes, a fourth impairment is present in both monostatic and bistatic deployments, namely the oscillator phase noise (PN). PN becomes particularly relevant at the millimeter wave (mmWave) frequency range and above, and it has been widely investigated for communication systems [25], [26]. In addition, it is also known to degrade sensing performance. For example, PN imposes challenges to important ISAC tasks such as clutter removal for effective sensing, e.g., in indoor environments [27], [28]. In frequency-modulated continuous wave (FMCW) radar systems, PN introduces random frequency deviations to the chirp signals, which ultimately lead to signal-to-noise ratio (SNR) loss and distort the intermediate frequency (IF) signal spectrum [29]. In the context of digital waveforms for radar sensing, the influence of PN on phase-modulated continuous wave (PMCW) was also analyzed for radar networks in [30] and [31]. The latter study demonstrated that PN leads to an SNR reduction due to degradation of the correlation properties of the adopted pseudorandom binary sequence (PRBS) and a stripe along the Doppler shift direction for each target in the radar image.

Manuscript received DD MM, 2024. The authors acknowledge the financial support by the Federal Ministry of Education and Research of Germany in the projects “KOMSENS-6G” (grant number: 16KISK123) and “Open6GHub” (grant number: 16KISK010). (*Corresponding author: Lucas Giroto de Oliveira.*)

L. Giroto de Oliveira, Y. Li, T. Zwick, and B. Nuss are with the Institute of Radio Frequency Engineering and Electronics (IHE), Karlsruhe Institute of Technology (KIT), 76131 Karlsruhe, Germany (e-mail: lucas.oliveira@kit.edu, yueheng.li@kit.edu, thomas.zwick@kit.edu, benjamin.nuss@kit.edu).

B. Geiger and L. Schmalen are with the Communications Engineering Laboratory (CEL), Karlsruhe Institute of Technology (KIT), 76187 Karlsruhe, Germany (e-mail: benedikt.geiger@kit.edu, laurent.schmalen@kit.edu).

In [32], [33], these effects were also briefly discussed for orthogonal frequency-division multiplexing (OFDM) radar and their causes attributed to a PN-induced common phase error (CPE) and intercarrier interference (ICI). Further studies such as [34]–[36] derive Cramér–Rao lower bounds (CRLBs) on the achievable accuracy of range and velocity, which is related to the Doppler shift, of a single radar target under PN influence. In [34], a strategy to estimate the PN parameters and use them to improve the accuracy of range and velocity estimates is also proposed. A detailed analysis of the PN influence on the SNR loss and distortion of radar images in both range and Doppler shift directions for different choices of OFDM waveform parameters and scenarios has, however, not been reported in the literature so far. This article aims to fill this gap by performing an analysis of sensing performance degradation due to PN in mmWave OFDM-based ISAC. For that purpose, the distortion of digital modulation constellation and the resulting degradation of target reflection main lobe and sidelobes levels in both range and Doppler shift directions of the radar image are adopted as performance metrics. Furthermore, the PN effect when changing individual OFDM signal parameters is analyzed, and both single- and multi-target scenarios with moving and static targets are addressed.

The contributions of this article can be summarized as follows:

- A thorough description and mathematical formulation of the effects of PN on mono- and bistatic OFDM-based ISAC architectures is given. This includes closed-form expressions showing the effects of PN-induced CPE and ICI on OFDM symbols in the frequency domain.
- An explanation of the relationship between PN and OFDM signal parameters, including the presentation of results to illustrate how digital modulation constellations are distorted is provided. In this sense, a comprehensive discussion on when CPE or ICI become the dominant PN-induced degradation to the OFDM-based ISAC system is made. To numerically quantify the constellation distortion, the error vector magnitude (EVM) is adopted as a performance parameter and quadrature phase-shift keying (QPSK), 16-quadrature amplitude modulation (QAM), 64-QAM, and 256-QAM modulations are considered, besides different OFDM signal parameter choices and PN levels.
- A comprehensive analysis of the PN-induced sensing performance degradation in mmWave OFDM-based ISAC systems with both flexible and 3GPP-compliant OFDM signal parameterization is conducted. For that purpose, the distortion of main lobe and sidelobes of targets in the range-Doppler shift radar images are evaluated by means of the peak power loss ratio (PPLR), peak sidelobe level ratio (PSLR), and integrated sidelobe level ratio (ISLR) parameters. The PPLR serves as a measure of power loss at the target reflection mainlobe, while PSLR and ISLR quantify the increase in the sidelobe level, which may eventually prevent the detection of the actual target or result in ghost targets. While these parameters are evaluated for a single target, they allow predicting the

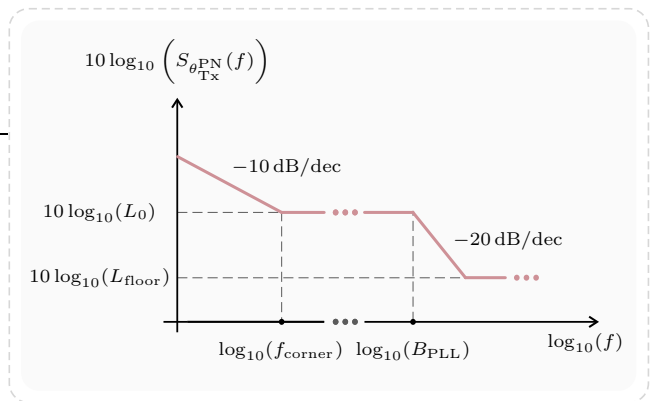


Fig. 1. Double-sided PSD profile of the assumed PN model for an PLL-based LO [25], [26], [32].

interaction between multiple targets in a radar image. In addition, the image signal-to-interference ratio (SIR) was also considered to analyze not only the distortion of the target reflection itself, but also the increase in the interference floor in the radar image caused by PN. The aforementioned parameters are also analyzed after CPE estimation and correction, which allows to partly compensate the PN effects at reasonable computational complexity costs.

The remainder of this article is organized as follows. Section II formulates the system model of an OFDM-based ISAC system under influence of PN. In Section III, a communication and radar sensing performance analysis of the aforementioned ISAC system under PN influence is performed. Finally, concluding remarks are presented in Section IV.

II. SYSTEM MODEL

In an OFDM-based ISAC system, constellation symbols \mathbf{d}_{Tx} belonging to a modulation alphabet \mathcal{M} such that $\mathbf{d}_{\text{Tx}}^{\text{OFDM}} \in \mathcal{M}^{NM \times 1} \subset \mathbb{C}^{NM \times 1}$ undergo serial-to-parallel (S/P) conversion and are reshaped into a discrete-frequency domain frame containing $N \in \mathbb{N}_{>0}$ subcarriers and $M \in \mathbb{N}_{>0}$ OFDM symbols. This frame is then transformed into the discrete-time domain via inverse discrete Fourier transforms (IDFTs) along the subcarriers at each OFDM symbol. A cyclic prefix (CP) of length $N_{\text{CP}} \in \mathbb{N}_{\geq 0}$ is then prepended to each of the aforementioned OFDM symbols. After parallel-to-serial (P/S) conversion on the resulting discrete-time domain frame, digital-to-analog (D/A) conversion with sampling rate F_s is performed on the resulting sample stream and the generated signal undergoes low-pass (LP) filtering, being then denoted as $x_{\text{BB}}(t) \in \mathbb{C}$. It is considered that the BB analog signal $x_{\text{BB}}(t)$ has bandwidth $B \leq F_s$, which results in an OFDM subcarrier spacing $\Delta f = B/N$. After up-converting $x_{\text{BB}}(t)$ to the carrier frequency $f_c \gg B$ with an in-phase/quadrature (I/Q) mixer, the RF analog signal $x_{\text{RF}}(t) \in \mathbb{C}$ expressed as

$$x_{\text{RF}}(t) = x_{\text{BB}}(t) e^{j[2\pi f_c t + \psi_{\text{Tx}} + \theta_{\text{Tx}}^{\text{PN}}(t)]} \quad (1)$$

is obtained. It is worth highlighting that $x_{\text{RF}}(t)$ is only modeled as a complex-valued signal for simplicity. In practice, it should be real-valued and both the frequency band of interest

centered at f_c and its mirror image centered at $-f_c$ should be considered when describing $x_{\text{RF}}(t)$ and the RF signals derived from it. Furthermore, the term $\psi_{\text{Tx}} \in \mathbb{R}$ in (1) denotes the transmitter carrier phase offset, and $\theta_{\text{Tx}}^{\text{PN}}(t) \in \mathbb{R}$ represents the transmitter PN that has a double-sided power spectral density (PSD) $S_{\theta_{\text{Tx}}^{\text{PN}}}(f) \in \mathbb{R}_{\geq 0}$ [37]. The profile of the aforementioned PSD is shown in Fig. 1 assuming that the local oscillator (LO) is implemented by using a phase-locked loop (PLL) [25], [26], [32]. In this figure, f_{corner} and B_{PLL} denote the flicker corner frequency and the PLL loop bandwidth, respectively. It is assumed that the PN PSD has a slope of -10 dB/dec until f_{corner} . Between f_{corner} and B_{PLL} , the PSD assumes the value L_0 , which is defined as the in-band PN level. After that interval, the PSD decays at a rate of -20 dB/dec until it reaches the PN floor L_{floor} . Both L_0 and L_{floor} are measured in rad^2/Hz . When the base-10 logarithm of the PSD of the PN is taken, the resulting unit becomes dBc/Hz. Based on these parameters, the transmit PN double-sided PSD can be mathematically described by [25], [32]

$$S_{\theta_{\text{Tx}}^{\text{PN}}}(f) = \frac{B_{\text{PLL}}^2 L_0}{B_{\text{PLL}}^2 + f^2} \left(1 + \frac{f_{\text{corner}}}{f} \right) + L_{\text{floor}}. \quad (2)$$

After being amplified by a power amplifier (PA) and radiated by the transmit antenna of the considered ISAC system, $x_{\text{RF}}(t)$ propagates through $P \in \mathbb{N}_{>0}$ labeled as $p \in \{0, 1, \dots, P-1\}$. Assuming that p th path is associated with attenuation α_p , delay τ_p , and Doppler shift $f_{\text{D},p}$, the receive captured signal by the receive antenna of the considered ISAC system can be denoted as $y_{\text{RF}}(t) \in \mathbb{C}$, which is expressed as

$$y_{\text{RF}}(t) = \sum_{p=0}^{P-1} \alpha_p x_{\text{RF}}(t - \tau_p) e^{j2\pi f_{\text{D},p} t}. \quad (3)$$

By substituting (1) into (3), (4) is obtained. After $y_{\text{RF}}(t)$ is amplified by a low-noise amplifier (LNA), it undergoes band-pass (BP) filtering and is down-converted with an I/Q

mixer. The resulting signal from the aforementioned down-conversion, $y_{\text{BB}}(t) \in \mathbb{C}$, can be expressed as

$$y_{\text{BB}}(t) = y_{\text{RF}}(t) e^{-j[2\pi f_c t + \psi_{\text{Rx}} + \theta_{\text{Rx}}^{\text{PN}}(t)]}, \quad (5)$$

where $\psi_{\text{Rx}} \in \mathbb{R}$ and $\theta_{\text{Rx}}^{\text{PN}}(t) \in \mathbb{R}$ denote the receiver carrier phase offset and the receiver PN time series in radians, respectively. In this article, it is assumed that the receiver LO is also derived from a PLL and that its PN has a double-sided PSD $S_{\theta_{\text{Rx}}^{\text{PN}}}(f) \in \mathbb{R}_{\geq 0}$ with the same profile as its counterpart at the transmitter side given by (2) and shown in Fig. 1. By substituting (4) into (5), the latter equation can be expanded as in (6). It is next assumed that $\theta_{\text{Tx}}^{\text{PN}}(t - \tau_p) - \theta_{\text{Rx}}^{\text{PN}}(t) \ll 1$, which is reasonable for typical PN levels in practice. Therefore, it holds that $\cos[\theta_{\text{Tx}}^{\text{PN}}(t - \tau_p) - \theta_{\text{Rx}}^{\text{PN}}(t)] \approx 1$ and $\sin[\theta_{\text{Tx}}^{\text{PN}}(t - \tau_p) - \theta_{\text{Rx}}^{\text{PN}}(t)] \approx \theta_{\text{Tx}}^{\text{PN}}(t - \tau_p) - \theta_{\text{Rx}}^{\text{PN}}(t)$, which allows further simplifying

$$e^{j[\theta_{\text{Tx}}^{\text{PN}}(t - \tau_p) - \theta_{\text{Rx}}^{\text{PN}}(t)]} = \cos[\theta_{\text{Tx}}^{\text{PN}}(t - \tau_p) - \theta_{\text{Rx}}^{\text{PN}}(t)] + j \sin[\theta_{\text{Tx}}^{\text{PN}}(t - \tau_p) - \theta_{\text{Rx}}^{\text{PN}}(t)] \quad (7)$$

as

$$e^{j[\theta_{\text{Tx}}^{\text{PN}}(t - \tau_p) - \theta_{\text{Rx}}^{\text{PN}}(t)]} \approx 1 + j[\theta_{\text{Tx}}^{\text{PN}}(t - \tau_p) - \theta_{\text{Rx}}^{\text{PN}}(t)]. \quad (8)$$

If, in addition, the phase terms associated with transmitter, receiver and the delay of the p th path are jointly represented by ψ_p such that

$$\psi_p = \psi_{\text{Tx}} - \psi_{\text{Rx}} - 2\pi f_c \tau_p, \quad (9)$$

then (6) can be rewritten as in (10). After LP filtering, the receive BB signal $y_{\text{BB}}(t)$ undergoes analog-to-digital (A/D) conversion with sampling rate F_s , which is associated with the sampling period $T_s = 1/F_s$. If $F_s > B$, it is assumed that digital low-pass filtering and downsampling to B is performed. Disregarding additive white Gaussian noise (AWGN), this yields the discrete-time domain sequence $y[s] \in \mathbb{C}$ that can be expressed as

$$y[s] = y_{\text{BB}}(t) \Big|_{t=sT_s}, \quad (11)$$

$$y_{\text{RF}}(t) = \sum_{p=0}^{P-1} \alpha_p \left[x_{\text{BB}}(t - \tau_p) e^{j[2\pi f_c(t - \tau_p) + \psi_{\text{Tx}} + \theta_{\text{Tx}}^{\text{PN}}(t - \tau_p)]} \right] e^{j2\pi f_{\text{D},p} t} \quad (4)$$

$$\begin{aligned} y_{\text{BB}}(t) &= \left\{ \sum_{p=0}^{P-1} \alpha_p \left[x_{\text{BB}}(t - \tau_p) e^{j[2\pi f_c(t - \tau_p) + \psi_{\text{Tx}} + \theta_{\text{Tx}}^{\text{PN}}(t - \tau_p)]} \right] e^{j2\pi f_{\text{D},p} t} \right\} e^{-j[2\pi f_c t + \psi_{\text{Rx}} + \theta_{\text{Rx}}^{\text{PN}}(t)]} \\ &= \sum_{p=0}^{P-1} \alpha_p x_{\text{BB}}(t - \tau_p) e^{j[\psi_{\text{Tx}} - \psi_{\text{Rx}} - 2\pi f_c \tau_p]} e^{j2\pi f_{\text{D},p} t} e^{j[\theta_{\text{Tx}}^{\text{PN}}(t - \tau_p) - \theta_{\text{Rx}}^{\text{PN}}(t)]} \end{aligned} \quad (6)$$

$$y_{\text{BB}}(t) = \left[\sum_{p=0}^{P-1} \alpha_p x_{\text{BB}}(t - \tau_p) e^{j\psi_p} e^{j2\pi f_{\text{D},p} t} \right] \left\{ 1 + j[\theta_{\text{Tx}}^{\text{PN}}(t - \tau_p) - \theta_{\text{Rx}}^{\text{PN}}(t)] \right\} \quad (10)$$

$$y_{n,m} = \left(\sum_{p=0}^{P-1} \alpha_p x_{\langle n-n_{\Delta,p} \rangle_N, m} e^{j\psi_p} e^{j2\pi f_{D,p}[m(N+N_{CP})+N_{CP}+n]/B} \right) \left[1 + j \left(\theta_{\text{Tx}}^{\text{PN}} ([m(N+N_{CP})+N_{CP}+n-n_{\Delta,p}]/B) - \theta_{\text{Rx}}^{\text{PN}} ([m(N+N_{CP})+N_{CP}+n]/B) \right) \right] \quad (12)$$

$$Y_{k,m} = \left[\sum_{p=0}^{P-1} \alpha_p X_{k,m} e^{j\psi_p} e^{-j2\pi k\tau_p B/N} e^{j2\pi f_{D,p}[m(N+N_{CP})+N_{CP}]/B} \right] + \frac{j}{N} \sum_{\kappa=-N/2}^{N/2} \left[\sum_{p=0}^{P-1} \alpha_p X_{\kappa,m} e^{j\psi_p} e^{-j2\pi \kappa \tau_p B/N} e^{j2\pi f_{D,p}[m(N+N_{CP})+N_{CP}]/B} \right] \times \sum_{n=0}^{N-1} \left(\theta_{\text{Tx}}^{\text{PN}} ([m(N+N_{CP})+N_{CP}+n-n_{\Delta,p}]/B) - \theta_{\text{Rx}}^{\text{PN}} ([m(N+N_{CP})+N_{CP}+n]/B) \right) e^{j2\pi(\kappa-k)n/N} \quad (13)$$

with $s \in \{0, 1, \dots, M(N+N_{CP})-1\}$. By performing S/P conversion on $y[s]$ and discarding the CP at each OFDM symbol, the discrete-time domain frame $\mathbf{y} \in \mathbb{C}^{N \times M}$ is obtained. Based on (10) and (11), the sample at the n th row and m th column of \mathbf{y} can be expressed as in (12) assuming that the Doppler-shift induced ICI is negligible for all P targets for simplicity. Without loss of generality, $n_{\Delta,p} = \tau_p B$ in this equation is assumed to be an integer to simplify the notation. In addition, $\langle \cdot \rangle_N$ is the modulo N operator. Next, the OFDM symbols contained in \mathbf{y} undergo discrete Fourier transforms (DFTs). This results in the discrete-frequency domain OFDM frame $\mathbf{Y} \in \mathbb{C}^{N \times M}$, whose sample at k th subcarrier, $k \in \{-N/2, 1, \dots, N/2-1\}$, at the m th OFDM symbol is expressed as in (13).

Considering a single path, i.e., $P=1$, and omitting the subscript p for the sake of simplicity, the OFDM frame \mathbf{Y} is split into the PN-free OFDM frame $\tilde{\mathbf{Y}} \in \mathbb{C}^{N \times M}$ and the PN-induced distortion to the OFDM frame $\boldsymbol{\eta}^{\text{PN}} \in \mathbb{C}^{N \times M}$. Consequently, the sample at the k th row and m th column of the PN-free OFDM frame $\tilde{\mathbf{Y}}$ is expressed as in (14), while the distortion at the same position of $\boldsymbol{\eta}^{\text{PN}}$ is expressed as in (15). Splitting (15) into the cases where the sum index κ is equal to or different than the analyzed subcarrier index k , i.e., $\kappa = k$ or $\kappa \neq k$, $\eta_{k,m}^{\text{PN,CPE}} \in \mathbb{C}$ and $\eta_{k,m}^{\text{PN,ICI}}$ are respectively obtained. These variables represent the PN-induced CPE and

the PN-induced ICI, which are expressed as in (16) and (17), respectively [38].

According to (16), the CPE causes a phase rotation due to the multiplication of $\tilde{Y}_{k,m}^p$ by $j\Phi_m^{\text{PN,CPE}}$, where $\Phi_m^{\text{PN,CPE}} \in \mathbb{R}$ is expressed as in (18) and does not depend on the subcarrier index k . Consequently, all subcarriers within the same OFDM symbol suffer the same phase rotation. While this can be corrected to a certain extent for communication by performing channel estimation and equalization with pilot subcarriers strategically placed in the OFDM frame, it may become an issue for radar sensing. This is due to the fact that the goal of radar sensing is to perform highly accurate channel estimation over consecutive OFDM symbols to allow estimating range and Doppler shift of targets [39]. While a phase rotation does not degrade the range profiles obtained at each OFDM symbol, it significantly impairs the Doppler shift estimation. This happens since the aforementioned process consists of converting the Doppler-shift induced phases into a Doppler shift estimate by performing one DFT over multiple OFDM symbols for. Since CPE alters the phase of each OFDM symbol, the obtained Doppler shift profiles will be distorted, presenting possible loss of the target peak power and increase of the sidelobe levels along the Doppler shift direction at the target range bin of the ultimately obtained range-Doppler shift radar image. The PN-induced ICI, in turn, already degrades

$$\tilde{Y}_{k,m} = \sum_{p=0}^{P-1} \alpha_p X_{k,m} e^{j\psi_p} e^{-j2\pi k\tau_p B/N} e^{j2\pi f_{D,p}[m(N+N_{CP})+N_{CP}]/B} \quad (14)$$

$$\eta_{k,m}^{\text{PN}} = \frac{j}{N} \sum_{\kappa=-N/2}^{N/2} \alpha X_{\kappa,m} e^{j\psi} e^{-j2\pi \kappa \tau B/N} e^{j2\pi f_{D,p}[m(N+N_{CP})+N_{CP}]/B} \times \sum_{n=0}^{N-1} \left(\theta_{\text{Tx}}^{\text{PN}} ([m(N+N_{CP})+N_{CP}+n-n_{\Delta,p}]/B) - \theta_{\text{Rx}}^{\text{PN}} ([m(N+N_{CP})+N_{CP}+n]/B) \right) e^{j2\pi(\kappa-k)n/N} \quad (15)$$

$$\eta_{k,m}^{\text{PN,CPE}} = \frac{j}{N} \tilde{Y}_{k,m} \sum_{n=0}^{N-1} (\theta_{\text{Tx}}^{\text{PN}} ([m(N + N_{\text{CP}}) + N_{\text{CP}} + n - n_{\Delta,p}]/B) - \theta_{\text{Rx}}^{\text{PN}} ([m(N + N_{\text{CP}}) + N_{\text{CP}} + n]/B)) \quad (16)$$

$$\eta_{k,m}^{\text{PN,ICI}} = \frac{j}{N} \sum_{\kappa=-N/2, \kappa \neq k}^{N/2} \tilde{Y}_{\kappa,m} \times \sum_{n=0}^{N-1} (\theta_{\text{Tx}}^{\text{PN}} ([m(N + N_{\text{CP}}) + N_{\text{CP}} + n - n_{\Delta,p}]/B) - \theta_{\text{Rx}}^{\text{PN}} ([m(N + N_{\text{CP}}) + N_{\text{CP}} + n]/B)) e^{j2\pi(\kappa-k)n/N} \quad (17)$$

$$\Phi_m^{\text{PN,CPE}} = \frac{1}{N} \sum_{n=0}^{N-1} (\theta_{\text{Tx}}^{\text{PN}} ([m(N + N_{\text{CP}}) + N_{\text{CP}} + n - n_{\Delta,p}]/B) - \theta_{\text{Rx}}^{\text{PN}} ([m(N + N_{\text{CP}}) + N_{\text{CP}} + n]/B)) \quad (18)$$

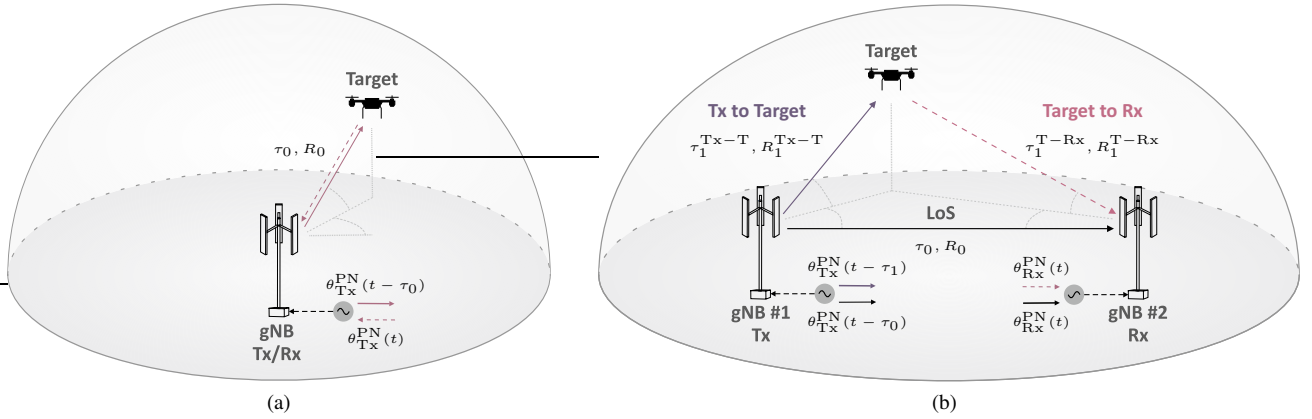


Fig. 2. Monostatic (a) and bistatic (b) ISAC scenarios. In the monostatic scenario in (a), a gNB performs monostatic sensing to detect a single target of index $p = 0$ at a range R_0 , which results in a single propagation path ($P = 1$) with propagation delay $\tau_0 = R_0/c_0$, where c_0 is the speed of light in vacuum. In this scenario, the effective transmit PN contribution is $\theta_{\text{Tx}}^{\text{PN}}(t - \tau_0)$, while the receive PN is $\theta_{\text{Rx}}^{\text{PN}}(t) = \theta_{\text{Tx}}^{\text{PN}}(t)$. In the bistatic ISAC scenario in (b), two gNBs communicate with one another through an LoS path of index $p = 0$, physical length R_0 , and propagation delay $\tau_0 = R_0/c_0$. In addition, the aforementioned gNBs also perform bistatic sensing of a single target of index $p = 1$ at a range R_1 , and with corresponding propagation delay $\tau_1 = R_1/c_0$. It holds that $\tau_1 = \tau_1^{\text{Tx-T}} + \tau_1^{\text{T-Rx}}$, where $\tau_1^{\text{Tx-T}} = R_1^{\text{Tx-T}}/c_0$, $\tau_1^{\text{T-Rx}} = R_1^{\text{T-Rx}}/c_0$, and $R_1^{\text{Tx-T}}$ and $R_1^{\text{T-Rx}}$ are respectively the ranges between transmitting gNB and radar target, and radar target and receiving gNB. In the bistatic case, the transmit PN contributions for the LoS path ($p = 0$) and the path associated with the radar target are $\theta_{\text{Tx}}^{\text{PN}}(t - \tau_0)$ and $\theta_{\text{Tx}}^{\text{PN}}(t - \tau_1)$, respectively. Unlike in the monostatic case, the receive PN contribution for both paths, $\theta_{\text{Rx}}^{\text{PN}}(t)$, has no correlation with $\theta_{\text{Tx}}^{\text{PN}}(t)$ in bistatic ISAC as different oscillators are used by the transmitting and receiving gNBs.

each OFDM symbol individually and not only when analyzing the whole frame as in the CPE case. The ICI causes loss of orthogonality between the subcarriers, reducing their effective signal-to-interference-plus-noise ratio (SINR) and degrading the performance of both OFDM-based communication and also sensing, resulting in peak power loss and sidelobe level increase in the obtained range profiles at each OFDM symbol and ultimately degrading the obtained range-Doppler shift radar image. According to [25], [32], [38], it is assumed that the CPE is the dominant PN-induced effect if $\Delta f/2 > B_{\text{PLL}}$, while ICI becomes the most relevant effect for $\Delta f/2 < B_{\text{PLL}}$. Since B_{PLL} values of 50 kHz [40], through around 150 kHz [41], and even up to 200 kHz [32] are reported for mmWave, both aforementioned cases can happen in practice, e.g., when subcarrier spacings ranging from 15 kHz to 120 kHz are used according to 3GPP specifications [42].

The influence of PN on the OFDM-based ISAC system

performance will depend on whether $\theta_{\text{Tx}}^{\text{PN}}(t)$ and $\theta_{\text{Rx}}^{\text{PN}}(t)$ are correlated. While correlated PN is observed in monostatic radar sensing due to the use of the same oscillator by both transmitter and receiver, the use of distinct oscillators results in non-correlated PN for bistatic radar sensing and communication. The aforementioned scenarios are depicted in Fig. 2, where a gNodeB (gNB) with full-duplex capability [12], [13] performs monostatic sensing in Fig. 2a and two gNBs perform simultaneous communication and bistatic sensing following the system concept from [20], [22] in Fig. 2b.

Besides quantifying the PN-induced impairments, there is also a growing interest in the literature regarding PN estimation and compensation. In OFDM-based optical communication, for instance, a dedicated continuous wave (CW) tone is simultaneously transmitted at the OFDM signal to fully estimate PN fully, i.e., both CPE and ICI [43]. A CW-based approach has also been proposed in [31], but it

is only applicable to PMCW-based radar sensing or ISAC. Further PN compensation strategies were proposed in [44]–[50]. Although these methods allow fully estimating the PN, they either require knowledge of the channel or perform joint PN and channel estimation. In ISAC applications, this would lead to rather high computational complexity as a dedicated estimate for each OFDM symbol would be needed, especially in scenarios with multiple targets with different Doppler shifts. In addition, the PN estimation would be biased towards estimating the PN of a dominant, reference path. This is, e.g., the case in bistatic sensing or communication with a line-of-sight (LoS) component between transmitter and receiver, as depicted in Fig. 2b. In monostatic sensing, a reference path is usually present due to coupling between transmit and receive antennas. Nevertheless, since this path has virtually zero range, the correlation between $\theta_{\text{Tx}}^{\text{PN}}(t)$ and $\theta_{\text{Rx}}^{\text{PN}}(t)$ will be maximum for it, and therefore the PN influence on this path will be significantly suppressed. Consequently, the transmit-receive coupled path cannot be used as a reference for CPE estimation. Using other targets at higher ranges also not a reliable strategy, as it cannot be ensured that they are static and their Doppler-shift-induced phases may also potentially bias the PN estimate.

While the PN-induced ICI cannot be efficiently combated, CPE can be estimated and corrected to a certain extent [51]. This partial PN compensation method is particularly efficient when the PN varies slowly within an OFDM symbol duration, which leads to dominant CPE over PN-induced ICI [52]. In OFDM-based communication, CPE estimation can be performed by using pilot subcarriers [53], at which the observed phase of the modulation symbol at the receiver side is compared with the one of the originally transmitted symbol. The aforementioned procedure can be mathematically described as

$$\hat{\Theta}_m^{\text{PN,CPE}} = \arg \left\{ \sum_{k=0}^{N-1} Y_{k,m} X_{k,m}^* \right\}, \quad (19)$$

where $\hat{\Theta}_m^{\text{PN,CPE}} \in \mathbb{R}$ is the CPE estimate for the m th OFDM symbol, $(\cdot)^*$, and $\arg\{\cdot\}$ returns the argument of a complex number. This estimate is then used for CPE correction on the receive frame \mathbf{Y} , producing the frame $\mathbf{Y}^{\text{corr}} \in \mathbb{C}^{N \times M}$ whose element at the k th and m th column is expressed as

$$Y_{k,m}^{\text{corr}} = Y_{k,m} e^{-j\hat{\Phi}_m^{\text{PN,CPE}}}. \quad (20)$$

In 5G New Radio (5G NR), for instance, the phase tracking reference signal (PT-RS) is used to estimate, track, and allow correcting PN-induced CPE [54]. The discussed CPE estimation and correction can improve the constellation shape and therefore communication and sensing performances. It is, however, is only suitable when there is a dominant, reference path, and therefore only suitable for bistatic ISAC architectures as previously discussed. As for the discussed full PN estimation strategies, the effectiveness of the CPE correction for sensing may also be limited if the PN changes rapidly, as multiple targets with rather low radar cross section (RCS) and at different ranges other than the one of the reference path are expected [55], [56]. These targets will experience

TABLE I
ADOPTED OFDM SIGNAL PARAMETERS

Carrier frequency (f_c)	26.2 GHz
Bandwidth (B)	1 GHz
No. of subcarriers (N)	{256, 512, 1024, 2048, 4096, 8192, 16384}
CP length (N_{CP})	{0, $N/4$, N }
No. of OFDM symbols (M)	{32, 128, 512, 2048}
Modulation alphabet	{QPSK, 16-QAM, 64-QAM, 256-QAM}

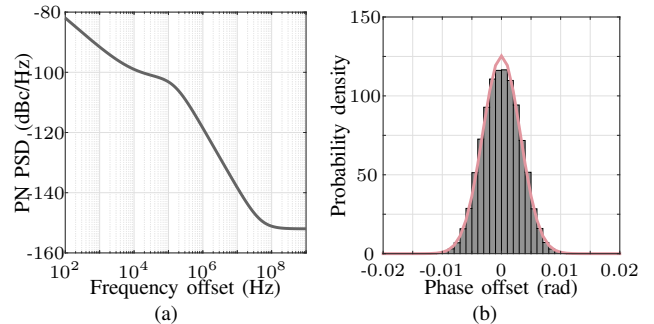


Fig. 3. Adopted PN model: (a) double-sided PN PSD and (b) PDF of the PN in the time domain.

significantly different PN realizations and consequently CPEs. In such cases, CPE estimation and correction is still desirable as it will improve the communication performance of the bistatic ISAC system. To decouple the CPE of the reference path and other targets, the CPE at a given OFDM symbol can be estimated based on the phase of the peak associated with the reference path after obtaining a channel impulse response (CIR) estimate from the pilot subcarriers.

Based on the presented OFDM-based ISAC system model under PN influence, the implications of the PN-induced degradation of communication and radar sensing performance in mono- and bistatic ISAC architectures as well as the effectiveness of the described CPE estimation and correction for communication and bistatic sensing are analyzed in Section III.

III. OFDM-BASED ISAC PERFORMANCE ANALYSIS

In this section, the performance of a mmWave OFDM-based ISAC system under PN is analyzed. Both monostatic and bistatic architectures are considered, and the PN-induced degradation of both communication and radar sensing performances is investigated. For that purpose, a corner frequency of $f_{\text{corner}} = 10$ kHz and a PLL loop bandwidth of $B_{\text{PLL}} = 150$ kHz were assumed, besides the in-band PN level of $L_0 = -105$ dBc/Hz and the PN floor $L_{\text{floor}} = -155$ dBc/Hz. The aforementioned parameters were chosen in order to simulate a PN PSD that is in between the specified ones of the E8257D PSG Microwave Analog Signal Generator from Keysight Technologies [41] for 20 GHz and 40 GHz. Those frequencies cover the initial part of the 5G NR Frequency Range 2 (FR2), which was used in the setups for ISAC measurements in previous works [24], [57]. In addition, the simulations in this sections consider the listed OFDM signal parameters in Table I, with the specific values used mentioned in each individual analysis.

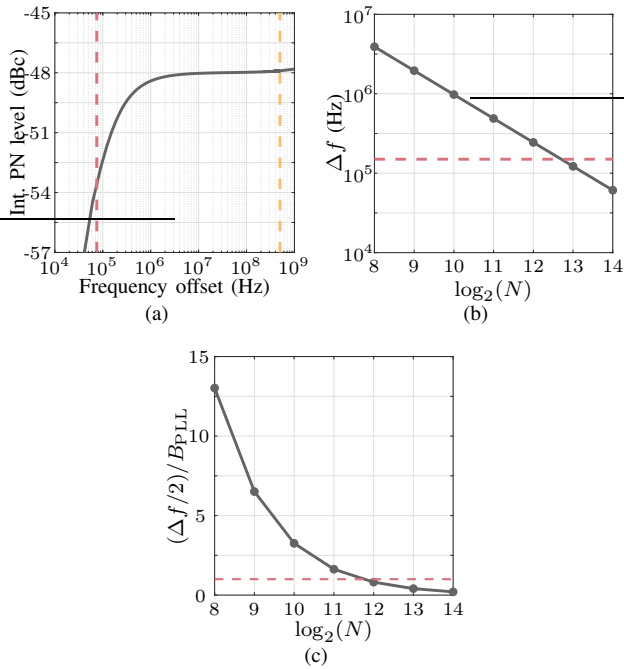


Fig. 4. Transition from CPE to ICI as dominant PN-induced effect: (a) integrated PN level as a function of frequency offset (double-sided) for the frequency range of interest, (b) subcarrier spacing Δf as a function of the number of subcarriers N , and (c) ratio between half of Δf and the PLL loop bandwidth B_{PLL} as a function of N (●). In (a) and (b), B_{PLL} is highlighted (---), whereas in (b), the ratio $(\Delta f/2)/B_{\text{PLL}} = 1$ below which ICI becomes more relevant than CPE is highlighted with the same line type. In addition, the offset of $B/2 = 500$ MHz is also highlighted in (a) (---), as this figure shows integrated double-sided PSD and therefore this offset corresponds to the bandwidth $B = 1$ GHz listed in Table I.

Based on the assumed parameters, the resulting double-sided PN PSD, which is assumed to be the same for both $S_{\theta_{\text{Tx}}^{\text{PN}}}(f)$ and $S_{\theta_{\text{Rx}}^{\text{PN}}}(f)$, and the probability density function (PDF) of the PN time series are shown in Figs. 3a and 3b, respectively. It is worth highlighting that this model is assumed for both transmitter and receiver. However, the interaction of both aforementioned PN terms will depend on whether a monostatic or bistatic ISAC architecture is assumed. In addition, the results in Fig. 4 reveal the relevance of B_{PLL} and its interplay with the subcarrier spacing Δf . Fig. 4a shows the integrated PN level as a function of the frequency offset, revealing that a PN level of -52.78 dBc, i.e., around 4.88 dB below the total PN level of -47.90 dBc, is accumulated by a frequency offset equal to B_{PLL} as expected from the discussion in Section II. This level is calculated by integrating the PN PSD occupied bandwidth assumed alongside the parameters listed in Table I, i.e., $B = 1$ GHz. In Fig. 4b, the subcarrier spacing Δf is shown as a function of the assumed numbers of subcarriers N in Table I. For better visualization, the N axis is shown in \log_2 scale, which results in $\log_2(\{256, 512, 1024, 2048, 4096, 8192, 16384\}) = \{8, 9, 10, 11, 12, 13, 14\}$. It is seen that only $N \leq 4096$ yield higher Δf than B_{PLL} . A more relevant ratio, which is the one between half of the subcarrier spacing, i.e., $\Delta f/2$, and B_{PLL} as discussed in Section II, is shown in Fig. 4c. It can be observed that $N \in \{256, 512, 1024, 2048\}$ yield $(\Delta f/2)/B_{\text{PLL}} > 1$, which implies that CPE is the dom-

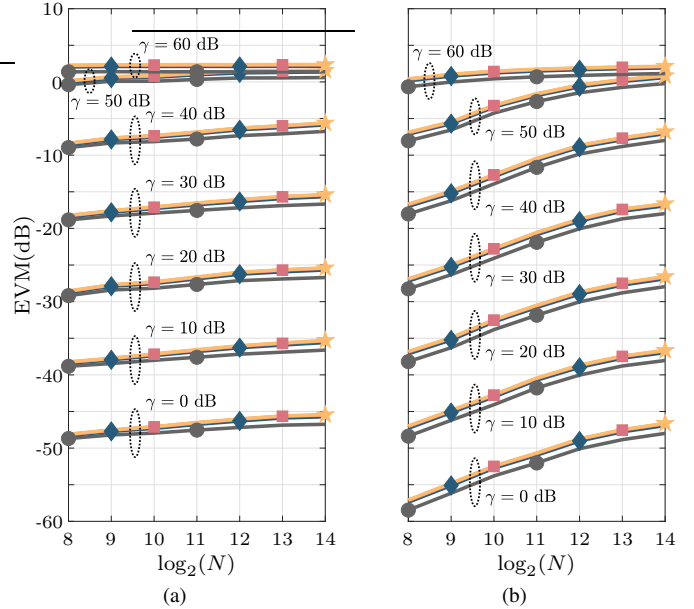


Fig. 5. EVM for $M = 128$ OFDM symbols, different numbers of subcarriers N and combined transmit and receive PN levels of -44.90 dBc, -34.90 dBc, -24.90 dBc, -14.90 dBc, -4.90 dBc, 4.90 dBc, and 14.90 dBc ($\gamma = 0$ dB, 10 dB, 20 dB, 30 dB, 40 dB, 50 dB, and 60 dB, respectively). In all cases, and QPSK (●), 16-QAM (◆), 64-QAM (■), and 256-QAM (★) modulations were considered. In (a), both ICI and CPE are entirely present, whereas in (b) CPE was estimated and corrected.

inant PN-induced effect for these numbers of subcarriers. However, for $N \in \{4096, 8192, 16384\}$, it holds that $(\Delta f/2)/B_{\text{PLL}} < 1$. Consequently, the PN-induced ICI becomes the dominant effect. This happens since the subcarrier spacing Δf decreases with increasing N , leading to more significant leakage of each subcarrier, which follows the shape of the PSD from Fig. 3a, on the frequency bins of its neighbors.

To evaluate the actual effect of PN on the performance of OFDM-based ISAC systems, simulation results focusing on the distortion of the constellation and radar sensing performance are presented in Sections III-A and III-B, respectively. Finally, remarks on the obtained simulation results in the two aforementioned sections are given in Section III-C.

A. PN-induced Distortion of Digital Modulation Constellation

For the analysis on the constellation distortion in an OFDM-based ISAC system under PN influence, a communication scenario where transmit and receive PN are uncorrelated is assumed. Assuming that the aforementioned PN contributions have the same level, their incoherent combination results in a 3 dB higher PN level as they are assumed to be uncorrelated Gaussian processes. In addition, an ideal channel model with a single path ($P = 1$) and null delay and Doppler shift (i.e., $\tau_0 = 0$ s and $f_{D,0} = 0$ Hz) is adopted. Since no intersymbol interference (ISI) happens in this scenario, $N_{\text{CP}} = 0$ is assumed.

Disregarding AWGN, Fig. 5a shows the achieved mean EVM over multiple PN realizations as a function of the number of subcarriers N for all digital modulations listed

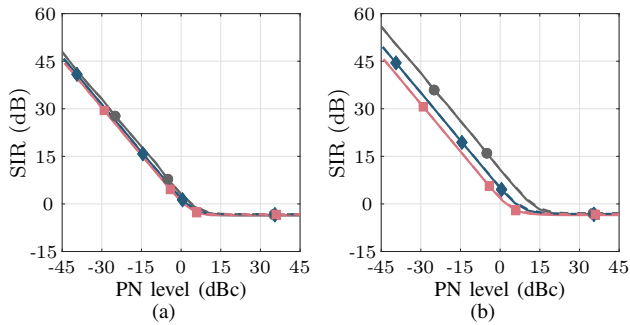


Fig. 6. SIR as a function of the combined transmit and receive PN level (a) without and (b) with CPE estimation and correction. Simulation results are shown assuming $N = 256$ and QPSK (— and ●), $N = 2048$ and QPSK (— and ◆), and $N = 16384$ and QPSK (— and ■). Results are also shown for 256-QAM and the aforementioned number of subcarriers, i.e., $N = 256$ (— and ●), $N = 2048$ (— and ◆), and $N = 16384$ (— and ■). In both cases, $M = 128$ OFDM symbols were considered.

in Table I. For the achieved results, the PN model from Fig. 3 was considered, and its original level of -47.90 dBc was increased by a factor $\gamma \in \mathbb{R}_{\geq 0}$ to showcase the induced degradation by PN at higher levels. Focusing on the $\gamma = 0$ dB case, i.e. the original PN model from Fig. 3 with a combined transmit and receive PN level of -44.90 dBc, it can be seen that the EVM degrades, i.e., increases, linearly along with increasing N , which is due to the decreasing subcarrier spacing Δf and resulting increased ICI effect. This becomes more pronounced for higher-order modulations, i.e., 16-QAM, 64-QAM, and 256-QAM, when compared to QPSK. This is due to the fact that the constellation points are relatively closer to one another in these modulations, and also because they do not have a constant envelope. Consequently, neighbor subcarriers may not have the same energy, leading to a more severe ICI effect. For PN increase factors of $\gamma = \{0, 10, 20, 30, 40, 50\}$ dB, which result in combined transmit and receive PN levels of -44.90 dBc, -34.90 dBc, -24.90 dBc, -14.90 dBc, -4.90 dBc, 4.90 dBc, respectively, the EVM is linearly degraded, i.e., increased, by the same factor γ . The EVM degradation only stops following the previously described pattern at a combined transmit and receive PN level of 14.90 dBc, which corresponds to $\gamma = 60$ dB. At this PN level, the EVM is constant regardless of the adopted number of subcarriers. In addition, the EVM increase trend observed for lower γ is not present for $\gamma = 60$ dB, as the EVM difference w.r.t. $\gamma = 50$ dB is smaller than 10 dB for all considered N values. This happens since even the highest Δf cannot prevent severe ICI at such PN level. Still considering an ideal channel model as well as the ideal case where all subcarriers are known at the receiver side, the EVM after CPE estimation and correction based on (19) and (20), respectively, is shown as a function of the number of subcarriers N is shown in Fig. 5b. It is observed that a significant EVM improvement of up to around 9.78 dB is observed for decreasing N in comparison with the results without CPE correction in Fig. 5a. This happens since CPE is more relevant for lower N , while higher N , and therefore lower subcarrier spacing Δf , leads to more pronounced PN-induced ICI that cannot be compensated with the adopted method.

Next, Fig. 6 shows the experienced SIR as a function of the combined transmit and receive PN level. For the performed simulations, $N \in \{256, 2048, 16384\}$, as well as QPSK and 256-QAM modulations were adopted. If CPE is not compensated, all considered N values and modulations yield similar performance, with SIR decreasing linearly from 45.72 dB on average at the PN level of -45 dBc until an average of 1.5 dB at the PN level of 0 dBc. In this zone, $N = 256$ performs around 1.5 dB better than $N = 2048$ and 3 dB better than $N = 16384$. At PN levels slightly higher than the latter, the linear behavior of the SIR is no longer observed, and a constant level is reached. In the case where CPE is estimated and corrected, higher SIR is observed for lower N in the linear SIR zone, which was already expected based on the EVM results from Fig. 5b. A significant SIR improvement, however, is only observed for $N = 256$ among the considered values. The maximum SIR improvement in the linear zone, which is of around 7.90 dB, is observed for $N = 256$. As for the other N values, lower SIR improvement is observed after CPE estimation and correction, being the difference for $N = 16384$ negligible. As in the case of Fig. 5b, the better performance improvement for lower N is due to the fact that the subcarrier spacing is higher and the ICI less pronounced in these cases. For all considered settings, a SIR of at least 15 dB is observed for combined transmit and receive PN levels equal to or lower than -15 dBc. At this PN level, reasonable communication performance in OFDM-based systems can still be achieved, e.g., as shown in [58]. For lower PN levels, critical SIR may be experience, leading to significant communication performance degradation. This is especially critical for bistatic ISAC, where reliable communication is require to reconstruct the transmit data and enable high-performance sensing [20], [22].

Examples on how the EVM and SIR degradation is related to changes in the constellation shape are shown for QPSK modulation considering -14.90 dBc ($\gamma = 30$ dB) in Figs. 7 and 8, which respectively address the cases without and with CPE estimation and correction. As expected from the results in Fig. 4, the obtained constellations show that the CPE is the dominating PN-induced degradation for $N \in \{256, 512, 1024, 2048\}$, whereas $N \in \{4096, 8192, 16384\}$ results in more significant ICI, which is evidenced by a more spurious, noise-like spreading of the constellation clusters.

B. Effects of PN on Radar Sensing

Considering the interaction of the PN at both transmitter and receiver as discussed in Section II, the total level of combined transmit and receive PN is shown in Fig 9 for both monostatic and bistatic ISAC architectures previously depicted in Fig. 2. Fig. 9a shows the combined PN level for monostatic radar sensing as a function of the monostatic range. For monostatic radar sensing, the transmit PN $\theta_{Tx}^{PN}(t)$ and the receive PN $\theta_{Rx}^{PN}(t)$ are correlated. As discussed in Section. II, the transmit PN contribution to the overall PN is $\theta_{Tx}^{PN}(t - \tau)$, where $\tau = 2R/c_0$ is the propagation delay associated with the monostatic range R . The receive PN contribution is in turn $\theta_{Rx}^{PN}(t) = \theta_{Tx}^{PN}(t)$. This results in a combined transmit

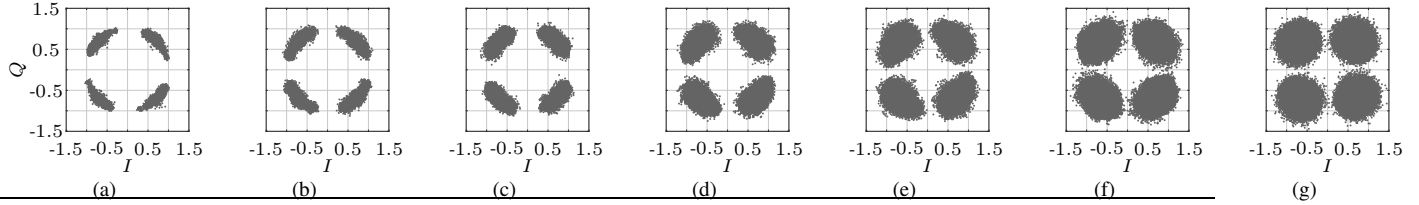


Fig. 7. Normalized receive QPSK constellations obtained for a combined transmit and receive PN level of -14.90 dBc ($\gamma = 30$ dB) and different numbers of subcarriers: (a) $N = 256$, (b) $N = 512$, (c) $N = 1024$, (d) $N = 2048$, (e) $N = 4096$, (f) $N = 8192$, and (g) $N = 16384$. In all cases, $M = 128$ OFDM symbols were considered.

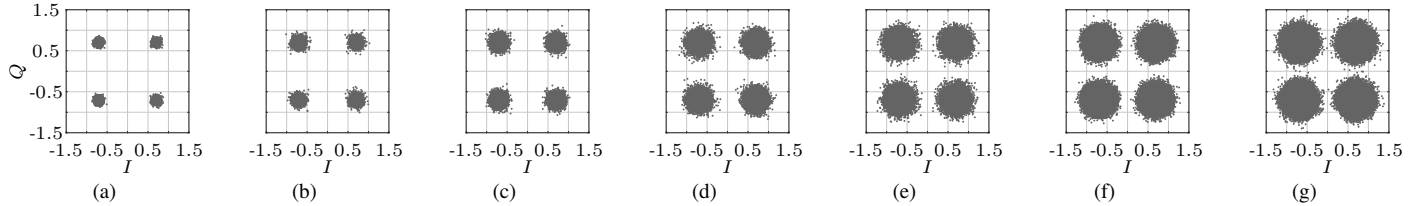


Fig. 8. Normalized receive QPSK constellations obtained after CPE estimation and correction for a combined transmit and receive PN level of -14.90 dBc ($\gamma = 30$ dB), $M = 128$ OFDM symbols, and number of subcarriers equal to: (a) $N = 256$, (b) $N = 512$, (c) $N = 1024$, (d) $N = 2048$, (e) $N = 4096$, (f) $N = 8192$, and (g) $N = 16384$.

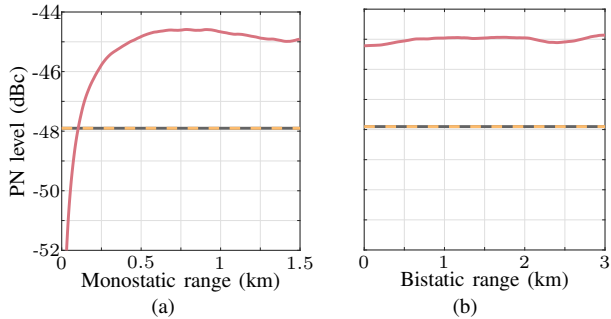


Fig. 9. Combined (—) transmit (—) and receive (---) PN level as a function of range: (a) monostatic sensing with correlated PN at transmitter and receiver and (b) bistatic sensing with uncorrelated PN. For communication, the same PN level is obtained as for bistatic sensing.

and receive PN level that tends to 0 rad^2 or $-\infty$ dBc for decreasing ranges or propagation delays, as

$$\lim_{\tau \rightarrow 0} [\theta_{\text{Tx}}^{\text{PN}}(t - \tau) - \theta_{\text{Tx}}^{\text{PN}}(t)] = 0. \quad (21)$$

For increasing ranges or delays, however, the $\theta_{\text{Tx}}^{\text{PN}}(t)$ and $\theta_{\text{Rx}}^{\text{PN}}(t)$ tend to become uncorrelated and their PN levels, which are both equal to -47.90 dBc, are simply added, resulting in the same combined transmit and receive PN level of -44.90 dBc observed in Section III-A. The bistatic sensing case in Fig. 9b shows a different behavior. Since $\theta_{\text{Tx}}^{\text{PN}}(t)$ and $\theta_{\text{Rx}}^{\text{PN}}(t)$ are uncorrelated as in the communication case discussed in Section III-A, since distinct oscillators are used by transmitter and receiver, the transmit and receive PN level add to -44.90 dBc regardless of the experienced range or propagation delay. For comparison, the achievable maximum unambiguous range for both monostatic and bistatic radar sensing, as a function of the number of subcarriers N and assuming $B = 1$ GHz as in Table I is shown in Fig. 10. The maximum unambiguous range is defined as $R_{\text{max,ua}} = N\Delta R$,

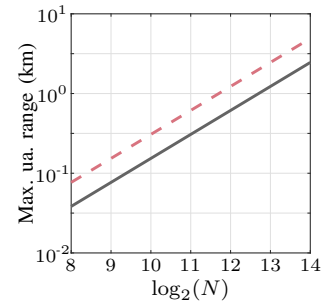


Fig. 10. Maximum unambiguous range as a function of the number of subcarriers N : monostatic sensing (—) and bistatic sensing (---).

where ΔR is the range resolution. For monostatic radar sensing, the maximum unambiguous range is defined as $R_{\text{max,ua}}^{\text{monost}} = N\Delta R^{\text{monost}} = N[c_0/(2B)]$ [39], while for bistatic radar sensing it is $R_{\text{max,ua}}^{\text{bist}} = N\Delta R^{\text{bist}} = N(c_0/B)$ [20]. The achieved results in Fig. 10 show that the maximum unambiguous range spans from 0.04 km to 2.45 km for the monostatic case, and from 0.08 km to 4.91 km for the bistatic case. This reveals that, for $N \leq 4096$, the whole achieved monostatic maximum unambiguous ranges profit from the transmit and receive PN correlation to a certain extent. Consequently, lower combined transmit and receive PN levels are experienced than in both the monostatic case for $N > 4096$ and the bistatic case regardless of N .

Next, to quantify the PN-induced degradation on monostatic and bistatic sensing in OFDM-based ISAC systems, the PPLR, PSLR, and ISLR parameters are used [39], [59], [60]. The first of the aforementioned parameters expresses the ratio between the main lobe power under PN influence and the ideally expected main lobe power without PN [61] after experiencing the radar processing gain of ideally NM under absence of PN [20], [39]. The latter parameters, i.e., PSLR and ISLR, express the ratio between the peak power of the highest sidelobe and

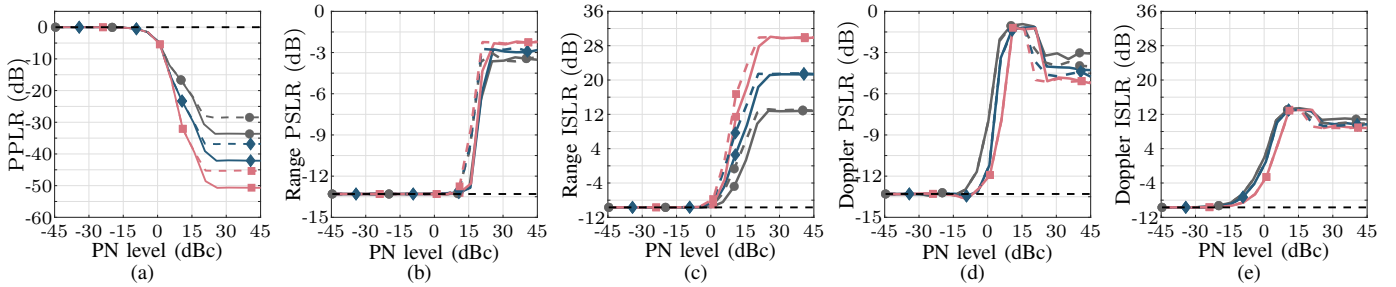


Fig. 11. PPLR (a), range PSLR (b) and ISLR (c), and Doppler shift PSLR (e) and ISLR (d) as functions of the combined transmit and receive PN level. Simulation results are shown for a static target assuming $N = 256$ and QPSK (— and ●), $N = 2048$ and QPSK (— and ◆), and $N = 16384$ and QPSK (— and ■). In addition, results are also shown for 256-QAM combined with the same aforementioned number of subcarriers, i.e., $N = 256$ (— and ●), $N = 2048$ (— and ◆), and $N = 16384$ (— and ■). In all subfigures, a CP length of $N_{CP} = N$ and $M = 128$ OFDM symbols were considered. In addition, the PPLR, PSLR and ISLR values for simulations without PN are also shown for comparison (---) and are the same regardless of the adopted modulation.

the main lobe and the ratio between the integrated sidelobe and main lobe powers [59], respectively. All three parameters are used to evaluate the PN effect on target reflections in a radar image under different settings. In addition, analysis using image SIR, which provides a measure between a target peak and the PN-induced interference in the radar image, as a performance parameter are also presented. The obtained results are discussed in Sections III-B1 through III-B6, for which parameter sets Table I are considered. The specifically adopted parameter values are explicitly mentioned in each of the aforementioned sections. Since the constellation distortion and SIR were analyzed in detail in Sec. III-A for all N and modulation alphabets from Table I, only $N \in \{256, 2048, 16384\}$ as well as QPSK and 256-QAM are henceforth considered for conciseness. This covers the cases $\Delta f/2 \gg B_{PLL}$, $\Delta f/2 \approx B_{PLL}$, and $\Delta f/2 \ll B_{PLL}$, respectively, as well as the two extremes of the considered modulation alphabets.

To focus only on the PN-induced impairments, self-interference is disregarded in the monostatic sensing case, and full knowledge of the transmit OFDM frame as well as perfect time, frequency and sampling frequency synchronization is assumed for bistatic sensing. For a more insightful analysis, PPLR and ISLR are calculated in both range and Doppler shift directions and, as in Section III-A, AWGN is not considered to highlight the PN effects. As in Section III-A, multiple PN level increase factors γ were considered in the simulations.

1) *Main and sidelobe distortion for different numbers of subcarriers and modulation alphabets:* To enable analyzing the radar sensing performance as a function of the number of subcarriers N and the modulation alphabet for a wide range of combined transmit and receive PN level, Fig. 11 shows the PPLR, range PSLR and ISLR, as well as Doppler shift PSLR and ISLR obtained for a static target. Since the monostatic and bistatic cases only differ in the transmit and receive PN correlation, which ultimately yields different combined PN levels as shown in Fig. 9, a generic case was simulated and the PN level was varied. This is later also done in Sections III-B2 and III-B3. In addition, $N \in \{256, 2048, 16384\}$, $N_{CP} = N$ to ensure that the maximum unambiguous range is measurable, as well as QPSK and 256-QAM were considered, besides $M = 128$ as in Section III-A. The obtained results in Fig. 11a reveal that the combined PN level result in negligible

PPLR until around -9.25 dBc. Afterwards, the PPLR degrades linearly until around 20.26 dBc, reaching a constant level that depends on the adopted N and modulation. These are -33.67 dB, -42.13 dB, and -50.66 dB for $N = 256$, $N = 2048$, and $N = 16384$, respectively, and QPSK modulation. For 256-QAM, the obtained PPLR values for high combined PN level were 5.28 dB higher, i.e., -28.47 dB, -36.85 dB, and -45.38 dB for $N = 256$, $N = 2048$, and $N = 16384$, respectively. From $N = 256$ to $N = 2048$ as well as from $N = 2048$ to $N = 16384$, the PPLR degrades 8.47 dB on average, i.e., it is worsened by a factor of approximately 7. This is close to the ratio 8 between $N = 16384$ and $N = 2048$, and also $N = 2048$ and $N = 256$, which also indicates the factor by which the subcarrier spacing Δf is decreased when increasing N , leading to more significant PN-induced ICI effect. An exact PPLR degradation by a factor of 8 is only not observed due to the form in which the PN level is spread over frequency as shown in Fig. 3a.

Regarding range PSLR, Fig. 11b shows that apart from a transition zone of a combined PN level between approximately 10.21 dBc and 25.73 dBc, where 256-QAM starts degrading at PN levels around 3 dB lower than QPSK, the choice of the modulation order does not influence the achieved PSLR. For combined transmit and receive PN levels from 25.73 dBc, $N = 256$, $N = 2048$, and $N = 16384$ result in constant range PSLR values of -3.42 dB, -2.97 dB, and -2.28 dB, respectively. In terms of range ISLR, a similar transition zone to the aforementioned one is observed in Fig. 11c. Afterwards, the same result is achieved regardless of the adopted modulation, and $N = 256$, $N = 2048$, and $N = 16384$ yield ISLR values of around 12.99 dB, 21.53 dB, and 30.02 dB, respectively. The difference of about 8.5 dB, which corresponds to worse ISLR by a factor of 7 between $N = 16384$ and $N = 2048$, as well as between $N = 2048$ and $N = 256$, is due to the increase in the number of samples used to represent the range axis of the radar image. Since the main lobe width is the same for all three aforementioned cases but the amount of samples containing sidelobes increases, the ISLR naturally degrades. This is, however, only observed since the high PN level results in significant ICI that severely increases the sidelobe level. Otherwise approximately the same ISLR is observed for all considered N values as is the case for combined PN levels

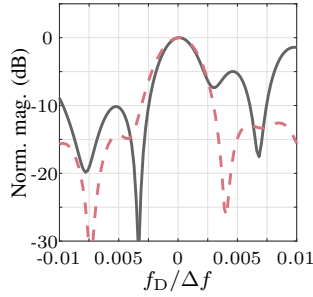


Fig. 12. Cut along the Doppler shift direction of bistatic range-Doppler radar images generated for a static target assuming $N = 2048$, $N_{CP} = 512$, $M = 128$, QPSK modulation, and rectangular windowing in both range and Doppler shift directions. Results are shown for 10 dBc ($\gamma = 54.90$ dB) (—) and 35 dBc ($\gamma = 79.90$ dB) (---). Since the considered PN levels lead to different PPLR and therefore peak heights in the radar image, the magnitudes are normalized to the respective static target peaks located at $f_D / \Delta f = 0$.

equal to or smaller than about 9.65 dBc in Fig. 11c. The achieved values show that the range PSLR and ISLR are only affected by rather high PN levels. This indicates that the PN-induced ICI can be suppressed by the radar processing gain as it is a Gaussian noise-like effect, and that CPE is the dominating source of PN-induced degradation of the sensing performance in OFDM-based ISAC for reasonable PN levels.

Finally, in terms of Doppler shift PSLR and ISLR, better performance is achieved by QPSK and smaller N in the region between -14.55 dBc and 11 dBc, where both PSLR and ISLR linearly degrade. The influence of the adopted modulation order on this tendency is small and becomes negligible with increasing N . Afterwards, both parameters improve with increasing combined transmit and receive PN level of up to about 26.06 dBc, where a constant level is achieved. This is illustrated in Fig. 12, where cuts along the Doppler shift direction of the radar images used to generate the results from Fig. 11 are shown. It can be observed that a combined PN level of 10 dBc ($\gamma = 54.90$ dB) results in higher sidelobes and a slightly narrower main lobe due to interaction with the sidelobes than in the case for 35 dBc ($\gamma = 79.90$ dB). As a result, this ultimately leads to worse PSLR and ISLR performances. The unexpected improved radar sensing performance with increasing PN level is due to the fact that the resulting PN PDF presents phase values outside the $(-\pi, \pi)$ range as shown in Fig. 13. Consequently, the PDF folds around and becomes a wrapped Gaussian distribution. This results in a changing PSLR and ISLR performance until the folding of the PDF becomes strong enough to give the PN PDF an uniform shape, which is when the PSLR and ISLR parameters present a constant level. It is, however, worth mentioning that such high combined transmit and receive PN levels should not be expected in practice, especially for mmWave systems. The aforementioned achieved PSLR levels are of approximately -3.02 dB, -4.07 dB, and -5.07 dB for $N = 256$, $N = 2048$, and $N = 16384$, respectively. As for ISLR, the aforementioned N values yield 10.88 dB, 9.57 dB, and 8.97 dB, respectively. The slightly better PSLR and ISLR along with N is due to the increasing ICI relevance in this case, which tends to make the PN-induced CPE less

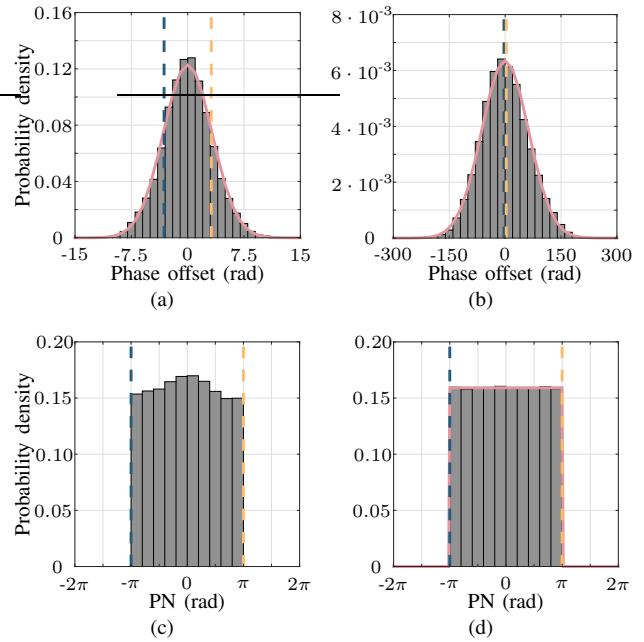


Fig. 13. PDF of the PN in the time domain: (a) 9 dBc ($\gamma = 53.90$ dB) and (b) 34 dBc ($\gamma = 78.90$ dB). In (c), and (d), the same cases as in (a) and (b) are respectively shown, after wrapping the phase between $-\pi$ (---) and π (---). While the PDFs in both (a) and (b) can be properly fitted by Gaussian distributions, and (d) by a uniform distribution, the PDF in (c) rather presents the form of a wrapped Gaussian distribution. For convenience, all obtained distribution fits are marked (—).

severe, although still significant, therefore resulting in less degradation of the DFT-based Doppler shift estimation that relies on the phases of consecutive OFDM symbols resulting from the target's Doppler shift.

2) *Main and sidelobe distortion for different numbers of OFDM symbols:* Setting $N = N_{CP} = 2048$ and focusing only on QPSK modulation, Fig. 14 shows results on the radar sensing performance degradation due to PN for $M \in \{32, 128, 512, 2048\}$ OFDM symbols. The obtained results show that increasing M results in a worse overall performance. A slight improvement in range PSLR and ISLR can indeed be seen in Figs. 14b and 14c, which is due to a higher radar processing gain against PN-induced ICI, which is the same for every OFDM symbol. However, with increasing M a higher number of OFDM symbols with PN-induced CPE is processed, which leads to a degradation of the PPLR proportional to M as observed in Figs. 14a. After a linear degradation zone from around -19.87 dBc, the PPLR reaches a constant level at 26.14 dBc. This level is equal to -36.58 dB, -42.08 dB, -47.76 dB, and -53.21 dB for $M = 32$, $M = 128$, $M = 512$, and $M = 2048$, respectively. This corresponds to an average PPLR degradation of 5.58 dB (factor of 3.61) from an M value to the next higher one, and it is close to the ratio of 4 between them. In addition, the Doppler shift PSLR and ISLR also degrade with increasing M due to increased CPE effect as seen in Figs. 14d and 14e. It can be seen that both curves present a similar behavior as their counterparts in Fig. 11. In terms of PSLR, constant levels of -5.10 dB, -3.85 dB, -3.3 dB, and -2.24 dB is observed for the considered M values in crescent order. The PSLR

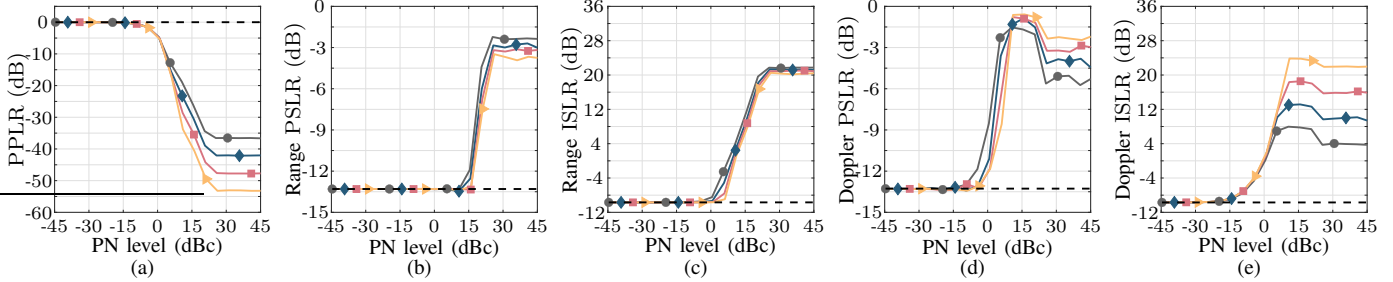


Fig. 14. PPLR (a), range PSLR (b) and ISLR (c), and Doppler shift PSLR (e) and ISLR (d) as functions of the combined transmit and receive PN level. Simulation results are shown for a static target assuming $N = 2048$, QPSK modulation, and $M = 32$ (\bullet), $M = 128$ (\blacklozenge), $M = 512$ (\blacksquare), and $M = 2048$ (\blacktriangleright). In all subfigures, a CP length of $N_{CP} = N$ was considered, and the PPLR, PSLR and ISLR values for simulations without PN are also shown ($-$).

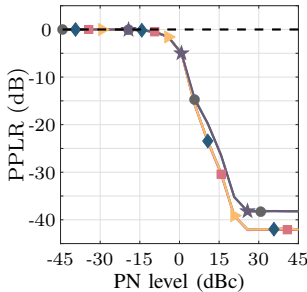


Fig. 15. PPLR as a function of the combined transmit and receive PN level. Simulation results are shown for a moving target assuming $N = 2048$, QPSK modulation, and $f_D = -0.5\Delta f$ (\bullet), $f_D = -0.1\Delta f$ (\blacklozenge), $f_D = 0$ (\blacksquare), $f_D = 0.1\Delta f$ (\blacktriangleright), and $f_D = 0.5\Delta f$ (\star). A CP length of $N_{CP} = N$ and $M = 128$ OFDM symbols were considered. For comparison, the PPLR values for simulations without PN or Doppler shift are also shown ($-$).

difference between consecutive values is, in all cases, smaller than 2 dB, and the PSLR values do not increase linearly with the ratio in which M is increased. Regarding Doppler shift ISLR, however, an average increasing step of 6.24 dB (factor 4.21) is observed for increasing M , which is close to the ratio of 4 between the considered consecutive M values. The observed ISLR values at the high PN level regime for $M = 32$, $M = 128$, $M = 512$, and $M = 2048$ are 3.85 dB, 10.01 dB, 15.80 dB, and 21.89 dB, respectively.

3) *Main and sidelobe distortion for moving targets:* In Fig. 15, radar sensing performance results are shown for $N = N_{CP} = 2048$, QPSK modulation, and Doppler shifts of $f_D \in \{0 \text{ Hz}, \pm 0.1\Delta f, \pm 0.5\Delta f\}$ to also cover scenarios with moving targets. Besides the static target case for $f_D = 0 \text{ Hz}$, which was already investigated in Fig. 11 and is only shown here as a reference, Doppler shifts of $f_D = \pm 0.1\Delta f$ are considered as they are assumed to result in tolerable Doppler-shift-induced ICI [39]. The Doppler shifts of $f_D = \pm 0.5\Delta f$, in turn, correspond to the maximum achievable unambiguous Doppler shift interval, which is obtained in the case where $N_{CP} = 0$ [20], [39]. Since the difference w.r.t. the range and Doppler shift PSLR and ISLR results from Fig. 11 was negligible, only PPLR is shown in Fig. 15. The achieved results shown that the PN-induced impairments combined have significantly more influence than the Doppler-shift-induced ICI on the radar sensing performance of the OFDM-based ISAC system. Only a slightly better PPLR is shown for $f_D = \pm 0.5\Delta f$, which is due to the fact that the Doppler-shift induced ICI may not always add constructively to its PN-induced counterpart. This

difference, however, only becomes visible for relatively high combined PN levels, i.e., above 5.70 dBc, and it is of around 4 dB when a constant PPLR level is achieved for a PN level of 25.74 dBc or higher.

4) *Main and sidelobe distortion for multiple moving targets:* The previous subsections show how PN degrades the PPLR, as well as range and Doppler shift PSLR and ISLR, of a single target under different settings. These parameters allow quantifying both the power loss at the main lobe and the sidelobe level increase in range and Doppler shift directions. To illustrate how this impacts the radar sensing performance of an OFDM-based ISAC system in multi-target scenarios, Fig. 16 shows range-Doppler shift radar images for one static and one moving target. In addition $N = 2048$, $N_{CP} = 512$, $M = 128$, and QPSK modulation were assumed. No AWGN was considered, and rectangular windowing was used in both range and Doppler shift processing. It can be seen that the sinc-shaped sidelobe pattern expected even without PN influence is clearly observable for a combined transmit and receive PN level of -44.90 dBc ($\gamma = 0 \text{ dB}$). For the considered higher combined PN levels of -14.90 dBc ($\gamma = 30 \text{ dB}$) and 4.90 dBc ($\gamma = 50 \text{ dB}$), the main lobe of both targets suffer from power loss as expected from the PPLR, and the Doppler shift sidelobes become much more relevant than their counterparts in the range direction, as expected from the analyses in the previous subsections.

Next, Fig. 17 shows range-Doppler shift radar images obtained with the same parameters adopted for Fig. 16, but applying Chebyshev windows with 100 dB sidelobe suppression in both range and Doppler shift directions. It can be seen in Fig. 17 that the windowing is only effective in range direction, as the PN-induced effect that plays a major role in range processing is ICI. As discussed in the previous subsections, the ICI produces a Gaussian noise-like effect that can be suppressed by the radar processing gain to some extent. Since this effect is additive, it does not reduce the effectiveness of windowing during range processing. As for windowing in the Doppler shift direction, it becomes little effective with increasing combined transmit and receive PN level as shown for -14.90 dBc ($\gamma = 30 \text{ dB}$) and 4.90 dBc ($\gamma = 50 \text{ dB}$). The reason for this is the severe CPE, which prevents the DFT-based estimation to generate a sinc-shaped Doppler shift profile even with rectangular windowing, e.g., as previously shown in Fig. 12. Consequently, the distorted, non-

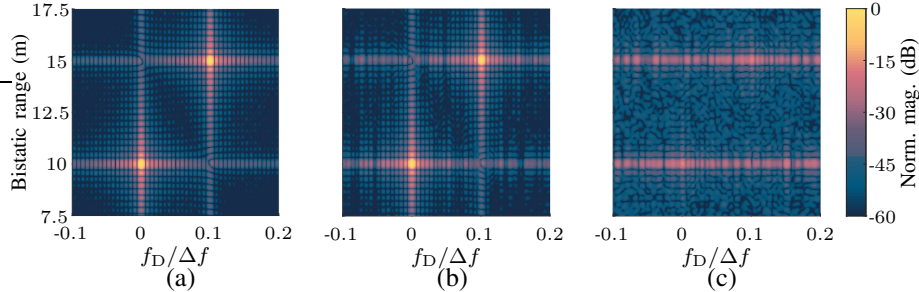


Fig. 16. Bistatic range-Doppler radar images obtained with $N = 2048$, $N_{CP} = 512$, $M = 128$, QPSK modulation, and rectangular windowing in both range and Doppler shift directions. Two targets were simulated, the first at 10 m and with a Doppler shift of 0 kHz and the second at 15 m and with a Doppler shift of $0.1\Delta f$ (which results in negligible ICI [39]). The considered combined transmit and receive PN levels in the simulations were (a) -44.90 dBc ($\gamma = 0$ dB), (b) -14.90 dBc ($\gamma = 30$ dB), and (c) 4.90 dBc ($\gamma = 50$ dB).

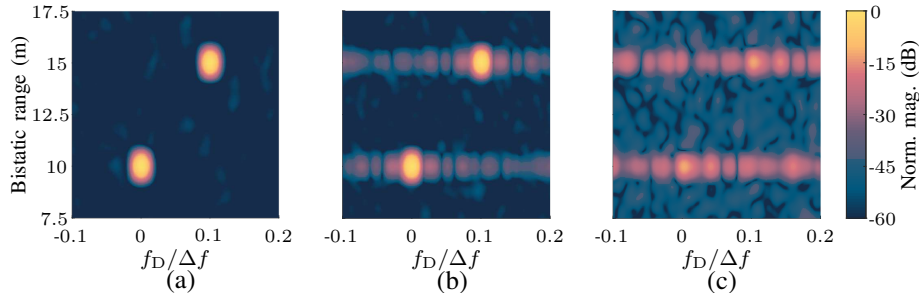


Fig. 17. Bistatic range-Doppler radar images obtained with $N = 2048$, $N_{CP} = 512$, $M = 128$, QPSK modulation, and Chebyshev windowing with 100 dB sidelobe suppression in both range and Doppler shift directions. Two targets were simulated, the first at 10 m and with a Doppler shift of 0 kHz and the second at 15 m and with a Doppler shift of $0.1\Delta f$ (which results in negligible ICI [39]). The considered combined transmit and receive PN levels in the simulations were (a) -44.90 dBc ($\gamma = 0$ dB), (b) -14.90 dBc ($\gamma = 30$ dB), and (c) 4.90 dBc ($\gamma = 50$ dB).

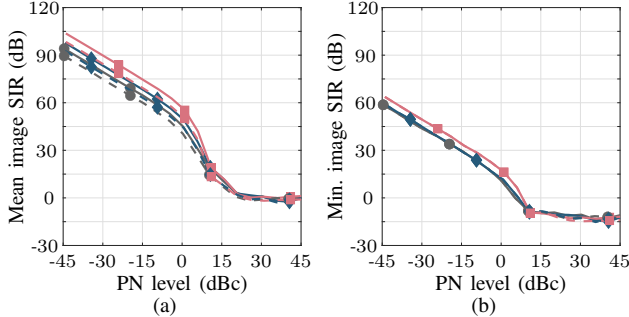


Fig. 18. Image SIR: (a) mean and (b) minimum values. In the performed simulations, a single static target was considered and $N = 256$ and QPSK (— and ●), $N = 2048$ and QPSK (— and ◆), and $N = 16384$ and QPSK (— and ■) were assumed. Results were also obtained for 256-QAM with $N = 256$ (— and ●), $N = 2048$ (— and ◆), and $N = 16384$ (— and ■). In all subfigures, a CP length of $N_{CP} = N$ and $M = 128$ OFDM symbols were considered.

decreasing Doppler shift sidelobe pattern cannot be effectively suppressed by Chebyshev windowing.

5) *Image signal-to-interference ratio*: To quantify the PN-induced radar image distortion as observed in Section III-B4, the image SIR as a function of the combined transmit and receive PN level is analyzed in Fig. 18. For simplicity, a single-target scenario is considered, and the same parameters from Section III-B1 are assumed. For the obtained results, Chebyshev window with 100 dB sidelobe suppression was used and the SIR was calculated as the magnitude ratio between the target reflection peak and the region outside the main lobe. In addition, both mean and minimum SIR values were

presented. These correspond to the average and minimum SIR calculated between the peak and each point outside the mainlobe, respectively.

The obtained mean SIR is shown in Fig. 18a. In this figure, a similar trend to what is experienced when performing communication over an ideal channel as shown in Fig. 6 is observed. However, the relationship between the SIR at the subcarrier level and the image SIR is not fully linear, as the PN-induced CPE and ICI are differently suppressed by the radar processing gain. Back to Fig. 18a, an approximately linear degradation is seen until a combined transmit and receive PN level of around 0 dBc is observed in Fig. 18a. Afterwards, the SIR decreases more steeply until a 0 dB floor is reached at around 20 dBc PN level. As expected, the minimum SIR shown in Fig. 18b tends to be significantly lower than the mean SIR in Fig. 18a, including the minimum SIR floor of around -15 dB at high PN levels. This happens since the minimum SIR is dominated by the Doppler shift sidelobes that are more severely degraded by CPE than the range sidelobes are by ICI, e.g., as discussed in Section III-B4. Compared to the results on mainlobe and sidelobe distortion in the previous subsections, it is seen that the image SIR is reduced even for rather low PN levels, while PPLR and range and Doppler PSLR and ISLR do not degrade before -15 dBc. At this PN level, however, mean and minimum image SIR values of approximately 60 dB and 30 dB or higher are respectively observed, which already represents non-negligible sensing performance degradation.

6) *Sensing performance under 3GPP specifications*: In the 3GPP technical report TR 38.803 [62], PN models for gNBs and user equipments (UEs) at 30 GHz were proposed. Based

TABLE II
ADOPTED OFDM SIGNAL PARAMETERS FOR THE SCENARIOS OF MONOSTATIC SENSING AT A SINGLE GNB (#1), BISTATIC SENSING BETWEEN TWO GNBs (#2), BISTATIC SENSING WITH A GNB AS A TRANSMITTER AND A UE AS A RECEIVER (#3), AND BISTATIC SENSING BETWEEN TWO UES (#4)

	Scenario #1	Scenario #2	Scenario #3	Scenario #4
Carrier frequency (f_c)	28 GHz	27.4 GHz	27.4 GHz	27.4 GHz
Frequency bandwidth (B)	1.6 GHz	190 MHz	190 MHz	190 MHz
No. of subcarriers (N)	12672	1584	1584	1584
CP length (N_{CP})	1600	112	112	112
No. of OFDM symbols (M)	384	1120	1120	1120
Digital modulation	QPSK	QPSK	QPSK	QPSK

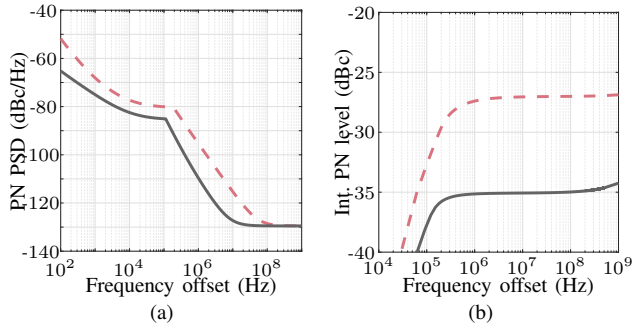


Fig. 19. 3GPP TR 38.803 PN model for a gNB (—) and a UE (---) at 30 GHz: (a) double-sided PN PSD and (b) integrated PN level as a function of frequency offset (also double-sided) for the frequency range of interest.

on these models, the double-sided PN PSDs shown in Fig. 19a and the integrated PN level were obtained. To analyze the sensing performance degradation imposed by these PN PSD profiles, four scenarios are considered. These are namely monostatic sensing at a single gNB, bistatic sensing between two gNBs, bistatic sensing with a gNB acting as a transmitter and a UE as a receiver, and bistatic sensing between two UEs, which are henceforth named Scenarios #1 to #4, respectively. For all scenarios, a single static target was considered, and the adopted OFDM signal parameters are listed in Table II. The parameters for Scenario #1 were suggested in [63], while those for Scenarios #2 to #4 were used for measurement-based ISAC demonstrations in [27], [28], [64]. Moreover, all of the adopted parameter sets comply with 3GPP specifications. Since there is only a slight difference between the adopted carrier frequencies and 30 GHz, the PN models from Fig. 19a were still used for Scenarios #1 to #4.

The resulting transmit, receive, and combined transmit and receive PN levels for each scenario, as well as the sensing performance degradation measured by PPLR, range PSLR and ISLR, Doppler shift PSLR and ISLR, as well as mean and minimum image SIR obtained for all four scenarios are listed in Table III. The achieved results show that the lowest combined transmit and receive PN level was -308.50 dBc in Scenario #1, which is due to the fact that monostatic sensing is performed and the transmit and receive PN correlation reduces the effectively experienced PN level. The achieved PN level was -26.99 dBc in Scenario #4, where bistatic sensing between two UEs is performed.

Overall, all considered scenarios yielded combined transmit

TABLE III
RESULTING PN-INDUCED SENSING PERFORMANCE DEGRADATION FOR SCENARIOS #1, #2, #3, AND #4

	Scenario #1	Scenario #2	Scenario #3	Scenario #4
Tx PN level	-34.45 dBc	-35.07 dBc	-35.07 dBc	-27.01 dBc
Rx PN level	-34.45 dBc	-35.07 dBc	-27.01 dBc	-27.01 dBc
Comb. Tx and Rx PN level	-308.60 dBc	-32.09 dBc	-26.43 dBc	-23.98 dBc
PPLR	0 dB	0 dB	-0.01 dB	-0.02 dB
Range PSLR	-13.30 dB	-13.30 dB	-13.30 dB	-13.30 dB
Range ISLR	-9.68 dB	-9.68 dB	-9.68 dB	-9.68 dB
Doppler PSLR	-13.30 dB	-13.27 dB	-13.27 dB	-13.26 dB
Doppler ISLR	-9.68 dB	-9.67 dB	-9.65 dB	-9.62 dB
Mean image SIR	148.28 dB	92.23 dB	86.15 dB	83.53 dB
Min. image SIR	100 dB	56.92 dB	53.72 dB	51.51 dB

and receive PN levels are all below -15 dBc, below which only negligible main and sidelobe level degradation is expected according to the presented results in Sections III-B1 to III-B4. This is confirmed by the remaining results in Table III, which show that negligible PPLR, range PSLR, and ISLR degradation in Scenarios #2 to #4 w.r.t. to the virtually PN-free case in Scenario #1 is observed. Regarding Doppler shift sidelobes, only a small variation in terms of PSLR is observed, besides a slight increase in ISLR from Scenarios #1 to #4 due to the increasing PN level. In terms of mean image SIR, high values are observed in all scenarios, which means that only negligible noise floor increase in radar images is expected. Regarding minimum SIR, only Scenario #1 presents no relevant SIR degradation due to non-suppressed Doppler shift sidelobes, which is simply explained by the rather low PN level in this case. As for Scenarios #2 to #4, the obtained minimum SIR values of 56.92 dB, 53.72 dB, and 51.51 dB show that non-negligible degradation in the Doppler shift direction is expected, although not severe.

Since only tolerable sensing performance degradation is observed in all four considered scenarios, it can be concluded that OFDM-based ISAC systems in the lower FR2 bands with 3GPP-compliant OFDM signal parameterization and PN levels equal to or lower than the models from TR 38.803 [62] present PN-robust sensing performance in both monostatic and bistatic architectures.

7) *Sensing performance with CPE compensation*: To analyze the effectiveness of the CPE estimation and correction according to (19) and (20) sensing performance, a bistatic scenario with a dominant, reference path only is assumed due to the reasons discussed in Section II. In addition, the same parameters adopted for the results in Fig. 11 discussed in Section III-B1 are considered. The obtained results in Fig. 20. Comparing with the results without CPE compensation from Fig. 11, it is seen that the PPLR becomes negligible for combined transmit and receive PN levels below 0 dBc, whereas a PPLR of -5 dB is achieved without CPE compensation. For higher PN levels, a PPLR floor is still reached, but less severe peak power losses are observed than in Fig. 11. On the one hand, it can also be seen that range PSLR is significantly improved, with better nearly ideal results for QPSK and smaller degradation than without CPE compensation for 256-QAM. On the other hand, range ISLR is not significantly

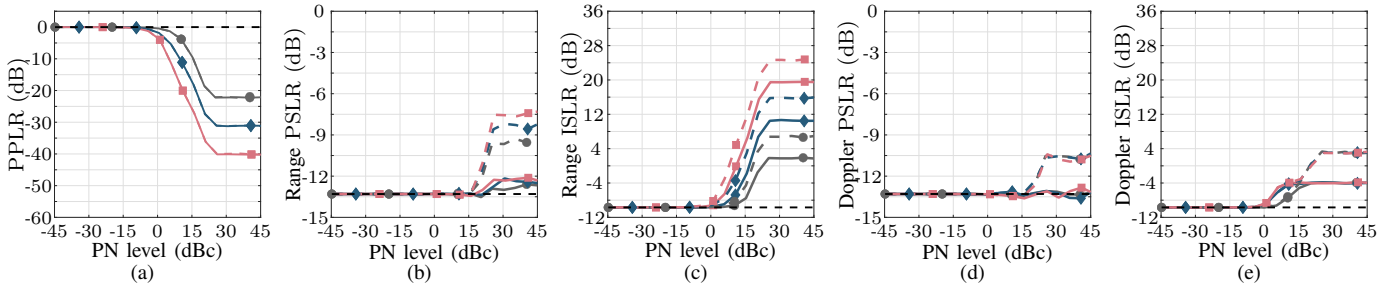


Fig. 20. PPLR (a), range PSRLR (b) and ISLR (c), and Doppler shift PSRLR (e) and ISLR (d) as functions of the combined transmit and receive PN level considering CPE estimation and correction from (19) and (20), respectively. The same scenarios as in Fig. 11 are considered, i.e., a single static target, CP length of $N_{CP} = N$, and $M = 128$ OFDM symbols are assumed, as well as $N = 256$ and QPSK (— and ●), $N = 2048$ and QPSK (— and ◆), and $N = 16384$ and QPSK (— and ■). Results are also shown for 256-QAM and the same aforementioned N values, i.e., $N = 256$ (— and ●), $N = 2048$ (— and ◆), and $N = 16384$ (— and ■). As in Fig. 11, the ideal PPLR, PSRLR and ISLR values without PN are also shown (---).

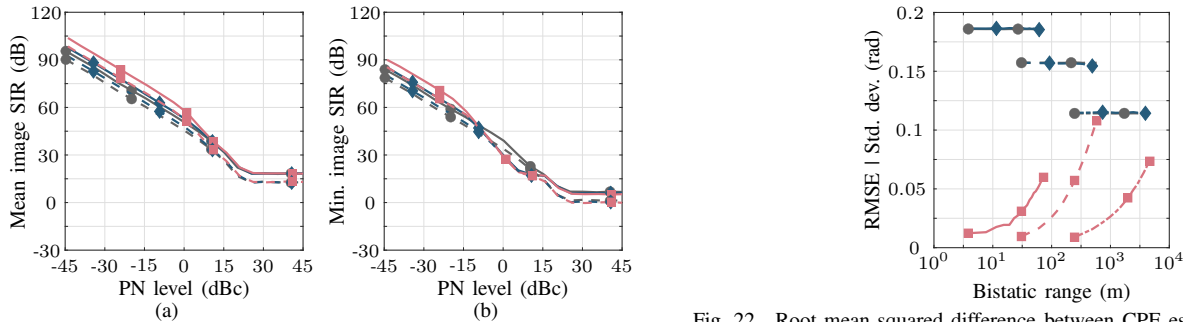


Fig. 21. Image SIR: (a) mean and (b) minimum values after CPE estimation and correction CPE estimation and correction from (19) and (20), respectively. As for Fig. 21, a single static target was considered and $N = 256$ and QPSK (— and ●), $N = 2048$ and QPSK (— and ◆), and $N = 16384$ and QPSK (— and ■) were assumed. Results were also obtained for 256-QAM with $N = 256$ (— and ●), $N = 2048$ (— and ◆), and $N = 16384$ (— and ■). In addition, a CP length of $N_{CP} = N$ and $M = 128$ OFDM symbols were considered.

Fig. 22. Root mean squared difference between CPE estimates of reference path and target reflection as a function of the range for $N = 256$ (— and ■), $N = 2048$ (--- and ■), and $N = 16384$ (--- and ■). For comparison, the CPE estimate standard deviation is shown for the reference path and $N = 256$ (— and ●), $N = 2048$ (--- and ●), and $N = 16384$ (--- and ●). In addition, the CPE estimate standard deviation of the target reflection is also shown for $N = 256$ (— and ◆), $N = 2048$ (--- and ◆), and $N = 16384$ (--- and ◆). As for the results shown in Figs. 20 and 21, a CP length of $N_{CP} = N$ and $M = 128$ OFDM symbols were considered.

improved as it is mainly caused by PN-induced ICI, which is not compensated. Finally, both Doppler shift PSRLR and ISLR experience significant improvement, also with better performance for QPSK compared to 256-QAM. As in the range case, some degradation is still experienced since the ICI also plays a role, although not dominant, in the Doppler shift estimation.

As for SIR performance with the adopted CPE estimation and correction approaches in the same scenario, the mean and minimum SIR results from Figs. 21a and 21b are respectively obtained. The results in Fig. 21a show that a slower SIR degradation is observed after 0 dBc than without CPE compensation previously shown in Fig. 18a. In addition, a mean image SIR floor of around 15 dB instead of 0 dB in the case without CPE compensation is reached at around 20 dBc. In Fig. 21b, significant SIR improvement is also observed, with at least 15 dB higher values than in the case without CPE correction in Fig. 18b.

When performing CPE estimation and correction in multi-target scenarios, the approaches described by (19) and (20) cannot be indiscriminately applied. Instead, CIR estimates can be obtained, e.g., based on pilot subcarriers, and the CPE for each target can be estimated as discussed in Section II. In practical applications, however, the radar targets tend to be rather

weak and not detectable without the additional processing gain of M provided by Doppler shift estimation. In addition, if the aforementioned targets are moving, their CPE will not be distinguishable from their Doppler-shift-induced phase. A solution is then to use the dominant, reference path to estimate the CPE and reuse this estimation for the whole OFDM symbol, which encompasses all possible targets. While this can improve the communication performance of the OFDM-based ISAC system, the CPE compensation effectiveness will be reduced for targets at higher ranges than the reference path, which will appear at 0 m in the bistatic radar image [20], [22], [24]. The reason for this is that such targets will experience a different realization of the combined transmit and receive PN $\theta_{Tx}^{PN}(t - \tau_p) - \theta_{Rx}^{PN}(t)$, which will lead to different CPEs. This is illustrated in Fig. 22, where the root mean squared difference between the CPE estimates for the reference path and a second target is analyzed and compared to the standard deviations of the individual CPE estimates. To obtain these results, Chebyshev windowing with 100 dB sidelobe suppression was applied to separate the reference path and the radar target in the obtained CIR estimates. In addition, only bistatic ranges between 5% and 95% of the maximum unambiguous range $R_{max,ua}^{bist} = N\Delta R^{bist} = N(c_0/B)$ were considered for the radar target to ensure that it is distinguishable from the reference path. Finally, the same SNR was assumed for both

the radar target at all ranges and the reference path in the obtained CIRs. Although not realistic, this ensures the same CPE estimation accuracy for the both of them to simplify the present analysis. The presented results in Fig. 22 show that, for short OFDM symbols, i.e., $N = 256$, the PN variation is fast enough to yield a non-negligibly biased CPE estimate for the radar target after only 10 m range in case the estimate for the reference path is reused. For higher N values, less CPE performance degradation is observed since the induced CPE, which is related with the term in (18) that tends to zero with increasing N as the transmit and receive PN terms also do, is reduced.

C. Remarks on simulation results

It is worth highlighting that the assumed PN model shown in Fig. 3 presents a comparatively low PN level compared to typical hardware. If communication or sensing is performed by a UE or between a gNB and a UE instead of the gNB-only scenarios depicted in Fig. 2, considerable higher PN levels can be observed as UE hardware is usually less advanced. This can be observed for lower FR2 bands below 30 GHz with 3GPP-compliant parameterization as discussed Section III-B6, where a combined transmit and receive PN level of -26.99 dBc ($\gamma = 17.91$ dB above the PN level from Fig. 3) was observed between two UEs in a bistatic ISAC architecture. One example where even higher PN level is observed is the 77 GHz setup in [31], whose PN PSD is somewhat similar to what is obtained increasing the level of the original PN model from Fig. 3 by $\gamma = 30$ dB. In this case, non-negligible EVM values are observed, which is graphically represented by the constellations in Fig. 7.

Based on the results from Sections III-B1 to III-B6, it can be concluded that non-negligible PN-induced sensing performance degradation in terms of mainlobe and sidelobe distortion is only observed for combined transmit and receive PN levels above -15 dBc. At this point, PPLR, Doppler shift PSLR, and Doppler shift ISLR are the first sensing performance parameters that start to degrade, e.g., as seen in Fig. 11a, d, and e. Although slightly more robust, range ISLR can also start degrading at this PN level depending on the OFDM signal parameterization, e.g., as shown in 14c. As for range PSLR, a significant higher robustness against PN compared to the other sensing performance parameters is observed, which non-negligible degradation being only observed for PN levels above around 11 dBc. At this point, the range processing gain N [20], [39] is not anymore sufficient to sufficiently suppress the PN-induced ICI, resulting in the fact that the highest sidelobe may either be significantly distorted or no longer be the nearest one to the main lobe, which ideally results in a PSLR of -13.30 dB.

Still regarding PN-induced mainlobe and sidelobe level degradation, Section III-B showed that, while the ICI may introduce a certain degree of degradation, the dominating impairment for sensing is tends to be the CPE, which is evidenced by the fact that Doppler shift PSLR and ISLR start degrading at lower combined transmit and receive PN levels than range PSLR and ISLR in all investigated settings. As a consequence,

target sidelobes in the Doppler shift direction tend to present irregular shape and notably higher level than in the range direction of obtained radar images. As previously mentioned, however, this effect is only observed for combined transmit and receive PN levels from around -15 dBc ($\gamma = 29.90$ dB) onwards. In addition, it becomes more severe with increasing number M of OFDM symbols used for radar processing. This happens since PN is not an additive noise, being therefore not linearly suppressed by a radar processing gain as it is the case for AWGN [20], [39].

If SIR is analyzed instead of mainlobe and sidelobe degradation, it can be seen that mean and minimum image SIR are limited to around 60 dB and 30 dB at a PN level of -15 dBc. Although no degradation of PPLR, range PSLR and ISLR, and Doppler shift PSLR and ISLR at this PN level is observed as previously discussed, non-negligible sensing performance degradation is experienced especially in the Doppler shift direction, where unwanted sidelobes that cannot be suppressed by windowing drive the minimum SIR value up. This is, e.g., illustrated by Fig. 17b, where windowing is no longer effective against Doppler shift sidelobes at a similar PN level, i.e. -14.90 dBc. Considering CPE estimation and correction approaches from (19) (20), respectively, significant sensing performance improvement was observed. In terms of mainlobe and sidelobe levels, only negligible degradation w.r.t. the PN-free case was observed for combined transmit and receive PN levels of 0 dBc or lower, which covers all possible practical scenarios. In terms of SIR, the most relevant difference was observed for the aforementioned PN level range, where at least 15 dB minimum SIR improvement was observed w.r.t. the case without CPE compensation, ensuring an SIR of at least 30 dB for all assumed sets of OFDM signal parameters.

It is worth mentioning that, if different PN PSD shapes are considered, which is the case when the parameters of either the transmit, receive or both PN contributions are different then the assumed ones in Section III, the most relevant parameters to evaluate the performance of OFDM-based ISAC systems will still be the combined transmit and receive PN level as well as the PLL loop bandwidth B_{PLL} , which defines the transition from CPE to ICI as the dominant PN-induced effect. Related analysis were in [26] to assess the performance of communication systems and [32], where a brief discussion on the effects of PN on stepped-carrier OFDM radar was presented.

IV. CONCLUSION

This article presented a sensing performance analysis of OFDM-based ISAC under influence of PN. In this context, an OFDM-based ISAC system model was formulated and the PN induced impairments to it mathematically described. It discussed that PN causes CPE and ICI. The first effect results in a distinct phase rotation to each OFDM symbol, while the latter effect already causes degradation within each OFDM symbol due to interference among subcarriers. More specifically, the performed analysis showed that monostatic sensing at lower ranges benefits from PN reduction, as transmit and receive PN are correlated and therefore add destructively

to a certain extent. In bistatic sensing, PN at the transmitter and receiver sides is uncorrelated and their combination equals to the sum of uncorrelated Gaussian processes, resulting in a 3 dB PN level increase regardless of the target range. It was also shown that higher-order modulations are more affected by PN, as they are more sensitive to CPE and ICI due to their dense constellations that also do not have a constant envelope.

After radar signal processing on the receive OFDM frame with the two aforementioned PN-induced impairments, power loss at the main lobe of radar target reflections is observed in the range-Doppler shift radar image. Furthermore, an increased sidelobe level in both range and Doppler shift directions is experienced, mainly due to ICI and CPE, respectively. These effects can severely degrade the quality of obtained radar images, possibly preventing the detection of actual targets or resulting in ghost targets. The latter issue is especially in the Doppler shift direction, since a distorted phase pattern will be fed to the DFT-based Doppler shift estimation. This results in a rather high sidelobe increase, which forms a stripe in the radar image that cannot be suppressed by windowing. It was also observed in the presented analysis that the an increasing number of subcarrier and increasing modulation order lead to more severe PN-induced sensing performance degradation, as the aforementioned ICI and CPE are intensified. In addition, an increasing number of OFDM symbols for radar processing leads to peak power loss and sidelobe level increase instead of additional processing gain as expected against AWGN, which is the case since PN is not an additive noise. Finally, it was shown that the mainlobe and sidelobe level degradation is only negligibly affected by the Doppler shift of targets.

The discussed PN-induced mainlobe and sidelobe level distortions, however, are only severe for rather high combined transmit and receive PN levels. Even in cases where little to no degradation of PPLR, range PSLR and ISLR, and Doppler shift PSLR and ISLR is observed, the SIR between a target reflection peak and the interference floor in the radar image is reduced due to the influence of PN. This effect is, however, tolerable until around -15 dBc, where the changes in the mainlobe and sidelobe levels are still negligible. More severe sensing performance degradation is therefore only expected in cases where hardware with less stringent specifications is used. For the specific case of OFDM-based ISAC systems in the lower FR2 bands that are parameterized in compliance with 3GPP specifications and use gNB or UE hardware with similar PN to what is specified by the 3GPP TR 38.803 [62], no severe sensing performance degradation is induced by PN, regardless of whether monostatic or bistatic architectures are adopted. Finally, it was observed that significant sensing performance enhancement is achievable with CPE estimation and correction. Although this does not fully compensates for the PN-induced effects, since ICI is not addressed, the main issue of unwanted sidelobes in the Doppler shift direction can be effectively compensated for expected combined transmit and receive PN levels in practice.

ACKNOWLEDGMENT

L. Giroto de Oliveira would like to thank Dr. Mateus de Lima Filomeno from the Federal University of Juiz de Fora,

Brazil, Dr. Silvio Mandelli and Marcus Henninger from Nokia Bell Labs, Stuttgart, Germany, as well as Tsung-Ching Tsai from the Karlsruhe Institute of Technology, Germany, for the valuable discussions.

REFERENCES

- [1] M. Chafii, L. Bariah, S. Muhaidat, and M. Debbah, "Twelve scientific challenges for 6G: Rethinking the foundations of communications theory," *IEEE Commun. Surv. Tut.*, vol. 25, no. 2, pp. 868–904, Second Quarter 2023.
- [2] F. Liu et al., "Integrated sensing and communications: Towards dual-functional wireless networks for 6G and beyond," *IEEE J. Sel. Areas Commun.*, vol. 40, no. 6, pp. 1728–1767, Jun. 2022.
- [3] H. Viswanathan and P. E. Mogensen, "Communications in the 6G era," *IEEE Access*, vol. 8, pp. 57 063–57 074, Mar. 2020.
- [4] N. Rajatheva et al., "White paper on broadband connectivity in 6G," *arXiv preprint arXiv:2004.14247 [eess.SP]*, Apr. 2020.
- [5] A. Kadelka, G. Zimmermann, J. Plachý, and O. Holschke, "A CSP's view on opportunities and challenges of integrated communications and sensing," in *2023 IEEE 3rd Int. Symp. Joint Commun. Sens.*, Mar. 2023, pp. 1–6.
- [6] V. Shatov et al., "Joint radar and communications: Architectures, use cases, aspects of radio access, signal processing, and hardware," *IEEE Access*, pp. 1–1, 2024.
- [7] A. Alkhateeb, S. Jiang, and G. Charan, "Real-time digital twins: Vision and research directions for 6G and beyond," *IEEE Commun. Mag.*, vol. 61, no. 11, pp. 128–134, Nov. 2023.
- [8] S. Imran, G. Charan, and A. Alkhateeb, "Environment semantic communication: Enabling distributed sensing aided networks," *arXiv preprint arXiv:2402.14766 [cs.IT]*, Feb. 2024.
- [9] R. Thomä, T. Dallmann, S. Jovanoska, P. Knott, and A. Schmeink, "Joint communication and radar sensing: An overview," in *2021 15th European Conf. Antennas Propag.*, Mar., pp. 1–5.
- [10] T. Wild, A. Grudnitsky, S. Mandelli, M. Henninger, J. Guan, and F. Schaich, "6G integrated sensing and communication: From vision to realization," in *2023 20th Eur. Radar Conf.*, Sept. 2023, pp. 355–358.
- [11] I. P. Roberts, Y. Zhang, T. Osman, and A. Alkhateeb, "Real-world evaluation of full-duplex millimeter wave communication systems," *IEEE Trans. Wireless Commun. (Early Access)*, pp. 1–1, Mar. 2024.
- [12] C. B. Barneto et al., "Full-duplex OFDM radar with LTE and 5G NR waveforms: Challenges, solutions, and measurements," *IEEE Trans. Microw. Theory Tech.*, vol. 67, no. 10, pp. 4042–4054, Oct. 2019.
- [13] C. B. Barneto, S. D. Liyanaarachchi, M. Heino, T. Riihonen, and M. Valkama, "Full duplex radio/radar technology: The enabler for advanced joint communication and sensing," *IEEE Wireless Commun.*, vol. 28, no. 1, pp. 82–88, Feb. 2021.
- [14] R. S. Thomä et al., "Cooperative passive coherent location: A promising 5G service to support road safety," *IEEE Commun. Mag.*, vol. 57, no. 9, pp. 86–92, Sept. 2019.
- [15] O. Kanhere, S. Goyal, M. Beluri, and T. S. Rappaport, "Target localization using bistatic and multistatic radar with 5G NR waveform," in *2021 IEEE 93rd Veh. Technol. Conf.*, Apr. 2021, pp. 1–7.
- [16] C. Mollén, G. Fodor, R. Baldemair, J. Huschke, and J. Vinogradova, "Joint multistatic sensing of transmitter and target in OFDM-based JCAS system," in *2023 Joint Eur. Conf. Netw. Commun. 6G Summit*, Jun. 2023, pp. 144–149.
- [17] R. Thomä and T. Dallmann, "Distributed ISAC systems – multisensor radio access and coordination," in *2023 20th Eur. Radar Conf.*, Sept. 2023, pp. 351–354.
- [18] V. Yajnanarayana and P. Geuer, "Bi-static sensing in OFDM wireless systems for indoor scenarios," *arXiv preprint arXiv:2403.04201 [cs.IT]*, Mar. 2024.
- [19] Z. Geng, "Evolution of netted radar systems," *IEEE Access*, vol. 8, pp. 124 961–124 977, Jul. 2020.
- [20] L. Giroto de Oliveira et al., "Bistatic OFDM-based joint radar-communication: Synchronization, data communication and sensing," in *2023 20th Eur. Radar Conf.*, Sept. 2023, pp. 359–362.
- [21] J. Pegoraro et al., "JUMP: Joint communication and sensing with unsynchronized transceivers made practical," *IEEE Trans. Wireless Commun. (Early Access)*, pp. 1–16, Feb. 2024.
- [22] D. Brunner et al., "Bistatic OFDM-based ISAC with over-the-air synchronization: System concept and performance analysis," *arXiv preprint arXiv:2405.04962 [eess.SP]*, May 2024.

- [23] A. Omri, M. Shaqfeh, A. Ali, and H. Alnuweiri, "Synchronization procedure in 5G NR systems," *IEEE Access*, vol. 7, pp. 41 286–41 295, Mar. 2019.
- [24] L. Giroto de Oliveira et al., "Pilot-based SFO estimation for OFDM-based bistatic integrated sensing and communication," *arXiv preprint arXiv:2407.07567 [eess.SP]*, Jul. 2024.
- [25] L. Smaini, *RF Analog Impairments Modeling for Communication Systems Simulation: Application to OFDM-based Transceivers*. John Wiley & Sons, Ltd, 2012.
- [26] M. R. Khanzadi, D. Kuylentierna, A. Panahi, T. Eriksson, and H. Zirath, "Calculation of the performance of communication systems from measured oscillator phase noise," *IEEE Trans. Circuits Syst. I, Reg. Papers*, vol. 61, no. 5, pp. 1553–1565, May 2014.
- [27] M. Henninger, S. Mandelli, A. Grudnitsky, T. Wild, and S. ten Brink, "CRAP: Clutter removal with acquisitions under phase noise," in *2023 2nd Int. Conf. 6G New.*, Oct. 2023, pp. 1–8.
- [28] M. Henninger, S. Mandelli, A. Grudnitsky, and S. ten Brink, "CRAP part II: Clutter removal with continuous acquisitions under phase noise," *arXiv preprint arXiv:2402.11939 [eess.SP]*, Feb. 2024.
- [29] S. Ayhan, S. Scherr, A. Bhutani, B. Fischbach, M. Pauli, and T. Zwick, "Impact of frequency ramp nonlinearity, phase noise, and SNR on FMCW radar accuracy," *IEEE Trans. Microw. Theory Tech.*, vol. 64, no. 10, pp. 3290–3301, Oct. 2016.
- [30] J. Kou, M. Bauduin, A. Bourdoux, and S. Pollin, "Distributed PMCW radar network in presence of phase noise," *arXiv preprint arXiv:2405.09680 [eess.SP]*, May 2024.
- [31] D. Werbunat et al., "On the synchronization of uncoupled multistatic PMCW radars," *IEEE Trans. Microw. Theory Tech. (Early Access)*, pp. 1–13, Feb. 2024.
- [32] B. Schweizer, D. Schindler, C. Knill, J. Hasch, and C. Waldschmidt, "On hardware implementations of stepped-carrier OFDM radars," in *2018 IEEE/MTT-S Int. Microw. Symp.*, Jun. 2018, pp. 891–894.
- [33] J. Aguilar, D. Werbunat, V. Janoudi, C. Bonfert, and C. Waldschmidt, "Uncoupled digital radars creating a coherent sensor network," *IEEE J. Microw.*, vol. 5, no. 3, pp. 459–472, Jun. 2024.
- [34] M. F. Keskin, H. Wymeersch, and V. Koivunen, "Monostatic sensing with OFDM under phase noise: From mitigation to exploitation," *IEEE Trans. Signal Process.*, vol. 71, pp. 1363–1378, Apr. 2023.
- [35] M. F. Keskin, C. Marcus, O. Eriksson, H. Wymeersch, and V. Koivunen, "On the impact of phase noise on monostatic sensing in OFDM ISAC systems," in *2023 IEEE Radar Conference (RadarConf23)*, May 2023, pp. 1–6.
- [36] V. Koivunen, M. F. Keskin, H. Wymeersch, M. Valkama, and N. González-Prelcic, "Multicarrier ISAC: Advances in waveform design, signal processing and learning under non-idealities," *arXiv preprint arXiv:2406.18476 [eess.SP]*, Jun. 2024.
- [37] P. W. van der Walt and W. Steyn, "Characterizing phase noise in self-referencing radar," *IEEE Aerosp. Electron. Syst. Mag.*, vol. 38, no. 12, pp. 4–13, Dec. 2023.
- [38] A. Garcia Armada, "Understanding the effects of phase noise in orthogonal frequency division multiplexing (OFDM)," *IEEE Trans. Broadcast*, vol. 47, no. 2, pp. 153–159, Jun. 2001.
- [39] L. Giroto de Oliveira, B. Nuss, M. B. Alabd, A. Diewald, M. Pauli, and T. Zwick, "Joint radar-communication systems: Modulation schemes and system design," *IEEE Trans. Microw. Theory Tech.*, vol. 70, no. 3, pp. 1521–1551, Mar. 2022.
- [40] D. Dhar, P. van Zeijl, D. Milosevic, H. Gao, and A. van Roermund, "Modeling and analysis of the effects of PLL phase noise on FMCW radar performance," in *2017 IEEE Int. Symp. Circuits Syst.*, May 2017, pp. 1–4.
- [41] Keysight Technologies. *E8257D PSG Microwave Analog Signal Generator* (2024). Accessed: Jun. 21, 2024. [Online]. Available: <https://www.keysight.com/us/en/assets/7018-01211/data-sheets/5989-0698.pdf>.
- [42] 3GPP, "3rd Generation Partnership Project; Technical Specification Group Radio Access Network; NR; Physical channels and modulation," 3rd Generation Partnership Project (3GPP), Tech. Rep. TS 38.211 V16.2.0 (2020-07), 2020.
- [43] S. Hussin, K. Puntsri, and R. Noe, "Efficiency enhancement of RF-pilot-based phase noise compensation for coherent optical OFDM systems," in *17th Int. OFDM Workshop 2012*, Aug. 2012, pp. 1–5.
- [44] R. Casas, S. Biracree, and A. Youtz, "Time domain phase noise correction for OFDM signals," *IEEE Trans. Broadcast.*, vol. 48, no. 3, pp. 230–236, Sept. 2002.
- [45] Q. Zou, A. Tarighat, and A. H. Sayed, "Compensation of phase noise in OFDM wireless systems," *IEEE Trans. Signal Process.*, vol. 55, no. 11, pp. 5407–5424, Nov. 2007.
- [46] V. Syrjala, M. Valkama, N. N. Tchamov, and J. Rinne, "Phase noise modelling and mitigation techniques in OFDM communications systems," in *2009 Wireless Telecommun. Symp.*, Apr. 2009, pp. 1–7.
- [47] S. Suyama, H. Suzuki, K. Fukawa, and J. Izumi, "Iterative receiver employing phase noise compensation and channel estimation for millimeter-wave OFDM systems," *IEEE J. Sel. Areas Commun.*, vol. 27, no. 8, pp. 1358–1366, Oct. 2009.
- [48] V. Syrjala and M. Valkama, "Analysis and mitigation of phase noise and sampling jitter in OFDM radio receivers," *Int. J. Microw. Wireless Technol.*, vol. 2, pp. 193 – 202, Apr. 2010.
- [49] R. Wang, H. Mehrpouyan, M. Tao, and Y. Hua, "Channel estimation, carrier recovery, and data detection in the presence of phase noise in OFDM relay systems," *IEEE Trans. Wireless Commun.*, vol. 15, no. 2, pp. 1186–1205, Feb. 2016.
- [50] A. Leshem and M. Yemini, "Phase noise compensation for OFDM systems," *IEEE Trans. Signal Process.*, vol. 65, no. 21, pp. 5675–5686, 2017.
- [51] J. Oh and T.-K. Kim, "Phase noise effect on millimeter-wave pre-5G systems," *IEEE Access*, vol. 8, pp. 187 902–187 913, Oct. 2020.
- [52] A. Armada and M. Calvo, "Phase noise and sub-carrier spacing effects on the performance of an OFDM communication system," *IEEE Commun. Lett.*, vol. 2, no. 1, pp. 11–13, Jan. 1998.
- [53] P. Robertson and S. Kaiser, "Analysis of the effects of phase-noise in orthogonal frequency division multiplex (OFDM) systems," in *Proceedings IEEE Int. Conf. Commun.*, vol. 3, Jun. 1995, pp. 1652–1657 vol.3.
- [54] Y. Qi, M. Hunukumbure, H. Nam, H. Yoo, and S. Amuru, "On the phase tracking reference signal (PT-RS) design for 5G new radio (NR)," in *2018 IEEE 88th Veh. Technol. Conf.*, Aug. 2018, pp. 1–5.
- [55] Z. Zhang et al., "A general channel model for integrated sensing and communication scenarios," *IEEE Commun. Mag.*, vol. 61, no. 5, pp. 68–74, May 2023.
- [56] J. Zhang et al., "Integrated sensing and communication channel: Measurements, characteristics, and modeling," *IEEE Commun. Mag.*, vol. 62, no. 6, pp. 98–104, Jun. 2024.
- [57] Y. Li et al., "User detection in RIS-based mmWave JCAS: Concept and demonstration," *IEEE Trans. Wireless Commun. (Early Access)*, pp. 1–16, Feb. 2024.
- [58] A. R. M. Ismail, M. Guenach, A. Bourdoux, and H. Steendam, "The effect of phase noise in OCDM," in *2023 IEEE Global Commun. Conf.*, Dec. 2023, pp. 3240–3245.
- [59] G. Lellouch, A. K. Mishra, and M. Inggs, "Design of OFDM radar pulses using genetic algorithm based techniques," *IEEE Trans. Aerosp. Electron. Syst.*, vol. 52, no. 4, pp. 1953–1966, Aug. 2016.
- [60] Z. Liao et al., "Pulse shaping for random ISAC signals: The ambiguity function between symbols matters," *arXiv preprint arXiv:2407.15530 [eess.SP]*, Jul. 2024.
- [61] J. Overvest, F. Jansen, F. Uysal, and A. Yarovoy, "Doppler influence on waveform orthogonality in 79 GHz MIMO phase-coded automotive radar," *IEEE Trans. Veh. Technol.*, vol. 69, no. 1, pp. 16–25, Jan. 2020.
- [62] 3GPP, "3rd Generation Partnership Project; Technical Specification Group Radio Access Network; Study on new radio access technology: Radio Frequency (RF) and co-existence aspects (Release 14)," 3rd Generation Partnership Project (3GPP), Tech. Rep. TR 38.803 V14.3.0 (2022-03), 2022.
- [63] S. Mandelli, M. Henninger, M. Bauhofer, and T. Wild, "Survey on integrated sensing and communication performance modeling and use cases feasibility," in *2023 2nd Int. Conf. 6G New.*, Oct. 2023, pp. 1–8.
- [64] P. Tosi, M. Henninger, L. Giroto de Oliveira, and S. Mandelli, "Feasibility of non-line-of-sight integrated sensing and communication at mmWave," *arXiv preprint arXiv:2406.12828 [eess.SP]*, Jun. 2024.